This is to certify that the
thesis entitled

EFFECTS OF THREE-DIMENSIONAL GEOMETRY ON
PENETRATION AND PERFORATION RESISTANCE

presented by

GEORGE JOSEPH COPPENS

has been accepted towards fulfillment
of the requirements for the

M.S. degree in Mechanical Engineering

Dr. Hui

Major Professor's Signature

7/22/04

Date

EFFECTS OF THREE-DIMENSIONAL GEOMETRY ON PENETRATION AND PERFORATION RESISTANCE

By

George Joseph Coppens

A THESIS

Submitted to
Michigan State University
in partial fulfillment of the requirements
for the degree of

MASTER OF SCIENCE

Department of Mechanical Engineering

2004

ABSTRACT

EFFECTS OF THREE-DIMENSIONAL GEOMETRY ON PENETRATION AND PERFORATION RESISTANCE

By

George Joseph Coppens

This thesis determined the penetration and perforation thresholds of laminated, stitched, and two- and three-dimensionally woven composite plates subjected to transverse impact. All composite plates were made from glass/epoxy prepreg tape so direct comparisons could be made about the effects of through thickness reinforcement on penetration and perforation thresholds. The effects of fiber angle were also studied. The laminated plates were made with various stacking sequences and had no additional through thickness reinforcement. The stitched plates were reinforced through the thickness with one-millimeter wide strips of prepreg. The two- and three-dimensional plates were hand woven using 12.7 mm wide strips of prepreg. The three-dimensional weaving technique was innovative in that it incorporated new fabric geometry to reinforce the plates through the thickness. A drop weight tester with an instrumented tup was used to impact the plates. The impact test data was used to determine the penetration and perforation thresholds. The three-dimensional woven plates had larger penetration and perforation thresholds than the laminated and two-dimensional plates as well as reduced delamination areas. The stitched plates had the largest penetration and perforation thresholds. Through thickness reinforcement increased penetration and perforation thresholds. The fiber angles of the laminated and three-dimensional plates also influenced their penetration and perforation thresholds.

DEDICATION

This work is dedicated to all my family and friends who have supported me during the years I have been in college.

ACKNOWLEDGMENTS

The assistance of Dr. Dahsin Liu was gratefully appreciated during my time at MSU. I would also like to thank my committee: Dr. Kwon, Dr. Lee, and Dr. Loos.

TABLE OF CONTENTS

LIST OF TABLES

LIST OF FIGURES

1. Introduction

Composite materials offer high strength-to-weight and stiffness-to-weight ratios making them excellent candidates for use in structures where strength must be maximized while minimizing weight such as high performance cars and racing boats. Composites can also be used as armor for civilian and vehicle applications due to their high energy absorption capabilities. Their role is to provide penetration resistance, impact energy dissipation, and damage containment [1]. Material selection of fibers and matrix, stacking sequence, and translaminar reinforcing techniques are some of the factors taken into account when designing composite armor.

Composite materials offer many benefits when compared to conventional metals. Composites can behave very poorly when subjected to transverse loading. One of the worst behaviors of composites is their tendency to delaminate when loaded transversely. Delamination can cause severe reductions in in-plane strength and stiffness, which can lead to failure of an entire structure. This drawback may be one of the biggest limiting factors on composite materials being used in more areas [2]. Other forms of damage are matrix cracking, fiber-matrix debonding, fiber microbuckling, fiber shear-out, and fiber fracture [3, 4].

Composite materials need to be more resistant to transverse loading. The amount of energy that composites can resist before penetration and perforation is reduced by delamination [5]. The motivation of this work was to increase penetration and perforation resistance by reducing delamination. There are two primary ways to achieve this goal; one is to use through thickness stitching and the other is to use woven fabrics.

1.1 Literature Survey

Laminated composite plates made from unidirectional fibers are susceptible to low velocity impact loads. Transverse damage resistance is especially poor since laminated composites have no through-thickness reinforcement. There have been many studies on laminated composites subjected to low velocity impact as evidenced by the review of Richardson and Wisheart [6]. Most studies agree that the most detrimental damage in composite laminates subjected to impact loading is delamination [2,7]. This type of damage can occur by relatively light impacts while the surface appears to be undamaged [8]. Laminated panels are still attractive because there are no crimp angles to reduce the in-plane properties and fiber volume fractions.

Many methods have been investigated with the goal of increasing the interlaminar fracture toughness of laminated composites. These include using toughened thermosetting matrices, translaminar reinforcement in the form of stitching, z-pinning, knitting, braiding, weaving, and modifying interfacial properties. Some studies have shown stitching can increase compression after impact strengths by 50% and increase Mode I fracture toughness by a factor of 30 [9]. Larsson found that stitching could increase impact delamination energy by more than 20 times when compared to unstitched plates [10]. This is because the stitching improves the delamination resistance energy by raising the Mode I interlaminar fracture resistance of the laminate, which makes it more difficult for a delamination crack to propagate between the fiber plies [11].

Stitching clearly has many benefits, including improved impact damage tolerance and improved delamination resistance to ballistic impact. However, there are problems associated with stitched composites. These include difficulties in stitching complex

shapes along with size and thickness restraints imposed by the sewing machines. Large purpose-built sewing machines require extremely high capital costs that are usually beyond the budget of most composite fabricators [12].

Stitching can also decrease in-plane stiffness and tensile and compressive properties by varying amounts [13]. The thread and needle used for stitching can damage the microstructure by breaking, spreading, and crimping the fibers around the stitch holes. Resin rich regions form around the stitch holes causing possible stress concentration zones [11].

Composite plates made from laminated two-dimensional (2D) woven fabric have received much attention. 2D fabric consists of plain, satin, twill, etc. weaving geometries. 2D fabrics offer improved impact resistance and damage tolerance because of their integrated nature and balanced in-plane properties [14]. Woven fabric laminates have been shown to have Mode I interlaminar fracture toughness of four to five times greater than laminates made of unidirectional fabric. This can be attributed to the roughness of the fabric, resin rich regions between the plies, and the ways in which crack propagation occurs [2]. The resin rich areas tend to arrest the interplay cracks and cause them to "jump" between undulations rather than extend continuously. The cracks also have difficulty in propagating because of the undulating paths that occur in the fabric [15]. Woven fabrics also have smaller damage areas after impact, thus they have higher residual compression strength when compared to unidirectional laminates. These strengths can be attributed to the more ductile and compliant nature of woven fabrics [2]. Siow and Shim studied plain weave carbon epoxy plates with a laminate sequence of $[0/90/-45/45/0/90]_S$. They found the damage mechanisms for woven laminates to be

mainly delamination and fiber breakage which were similar to unidirectional laminates [16].

Three-dimensional (3D) composites have become very popular based on their greater delamination resistance, ballistic damage resistance, and impact damage tolerance. Weaving, braiding, stitching, and knitting are all methods for producing 3D composites. The impact energy needed to initiate damage in 3D woven carbon-bismaleimide composites is up to 60% higher than in a laminated counterpart of the same materials. Their Mode I interlaminar fracture toughness values can be 6-20 times higher than unidirectional composites. This group of composites gets their superior properties from the through-thickness binder yarns which can arrest or slow the growth of delamination cracks [12].

Many of the in-plane properties of 3D composites are usually inferior to laminated counterparts when an equivalent amount of fibers are aligned in the load direction. Stiffness values are similar to 2D fabrics but their tension and compression strengths may be lower by 15-20%. The strength reduction is due to the crimping and distortion of in-plane fibers by the binder yarns [12].

1.2 Scope of Current Study

This thesis research attempted to determine the energy required to cause penetration and perforation of glass/epoxy composite plates subjected to low velocity impact. The use of only one material allowed direct correlations to be made between fabric geometry and penetration and perforation resistance.

Laminated, stitched, 2D woven, and 3D woven geometries were tested. The laminated geometry was used to produce a baseline for comparing the other geometries to. The

laminated plates had no through-thickness reinforcement. The stitched plates were reinforced through the thickness by thread. Each piece of glass/epoxy that made up the 2D woven plate was reinforced, but the pieces were only joined by matrix material. The 3D woven geometry used the fibers, as well a matrix, to join all of the plies together through the thickness.

1.3 Organization

This thesis is divided into six chapters. Chapter 1 introduces composite materials along with their advantages and drawbacks. The reasons for conducting this study are discussed. Chapter 1 also provides a literature survey of recent work performed on laminated, stitched, 2D woven and 3D woven composite materials. Chapter 2 discusses the materials and methods used for fabricating the composite plates. The procedure used to cure the plates is included along with the specifications of the composite plates. Chapter 3 includes the equipment and procedures used to test the composite plates and the equations used to calculate their performance. Chapter 4 discusses the energy profile method used to determine the penetration and perforation resistance of the composite plates. The problems encountered while testing along with their solutions are presented. The results of laminated specimens are used to discuss the problem solutions. Chapter 5 presents selected results from this study along with discussions on angle effect and the effects of through-thickness reinforcement. Chapter 6 concludes the entire project and offers recommendations for future studies.

2. Fabrication

The following sections discuss the material and methods used to construct the composite plates. The autoclave cure cycle for the thermosetting composite material is also presented.

2.1 Material

All composite plates constructed for this study were made from Scotchply type 1003-A tape which was a non-woven, unidirectional fiberglass tape pre-impregnated (prepreg) with an epoxy matrix. The prepreg tape came on a 300 mm (12") wide roll with a total length of 66 m (72 yards). The prepreg tape was sealed inside a plastic bag and stored in a freezer when not being used. The sealed plastic bag containing the prepreg tape was removed from the freezer and allowed to warm for approximately one hour prior to use. Leaving the prepreg tape in the sealed plastic bag while warming prevented condensation from forming on the composite material.

2.2 Manufacturing

2.2.1 Laminated Plates

Laminated composite plates were constructed from twelve pieces of prepreg tape. Each piece was 300 mm x 300 mm, namely 0° and 90° ply. The angled plies were cut by using patterns. The patterns were placed on the prepreg tape and then cut around. The plies were then stacked together to create the laminated plates, as shown in Figure 2-1. An optical microscope image of the actual cross section of a portion of a $L[(0/90)_6]$ specimen at a magnification of 120X is shown in Appendix A. The plates had a stacking sequence of $[0/\theta/0/\theta/0/\theta/0/\theta/0/\theta/0/\theta]$ with θ being equal to 7.5, 15, 30, 45, or 90 degrees.

They were designated as L[(0/θ)$_6$]. The plates were unsymmetric and had dimensions of 300 mm x 300 mm.

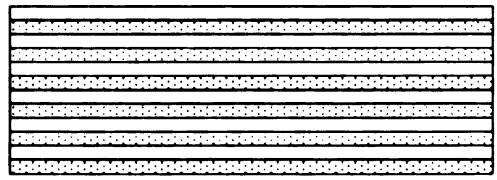

Figure 2-1:Side view of laminated plate.

Special tailoring was required for the angled plies where θ equaled 7.5, 15, 30, or 45 degrees. Gaps were created in the angled plies since the tape was only 300 mm wide. Figure 2-2 illustrates how the prepreg tape was cut to create the pieces labeled A and C. The horizontal lines were used to represent the direction of the fibers. The area enclosed by the dashed lines, labeled A', was the gap. Piece A was used to fill the gap to create the 300 mm x 300 mm angled ply. The length of each ply and the cutting lines were determined in the CAD program that was used to create the patterns. The fiber continuity was important when creating the angled plies. Only certain pieces of the pattern could be used to fill gaps. Area B could have been rotated 90° clockwise and used to fill gap A'

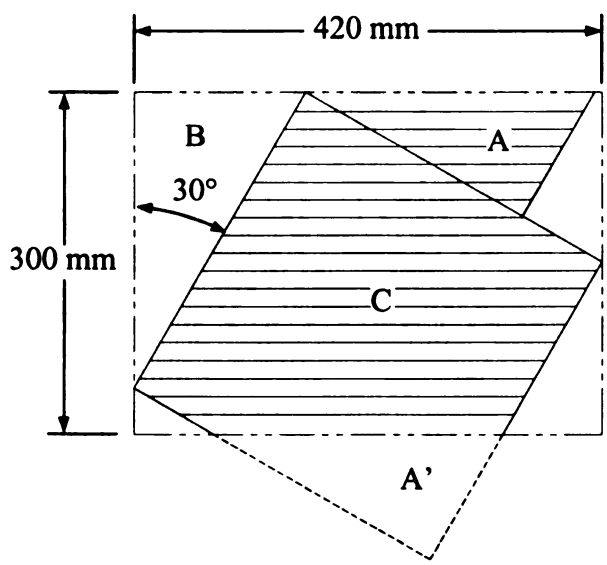

Figure 2-2:Cutting pattern for 30° ply.

but the fiber orientation would have been wrong. In addition, the plies were cut so that edges of all gaps were parallel to the fiber direction.

2.2.2 Stitched Plate

The stitched plate was based on a laminated stacking sequence of $L[(0/90)_6]$ which was unsymmetric. The stitching was done by hand using a needle and 1 mm wide strips of prepreg for thread. A horizontal stitching pattern was used as shown in Figure 2-3a. The nodes in the figure represent the stitching points for a portion of the plate. The solid and dashed lines represent the thread above and below the plate, respectively. The path of the thread through the plate is shown in Figure 2-3b. An optical microscope image of the actual cross section of a portion of a $S[(0/90)_6]$ specimen at a magnification of 120X is shown in Appendix A. The distance between each stitch as well as each row of stitching was 12.7 mm forming unit cells of 12.7 mm x 12.7 mm. The stitched plate was designated as $S[(0/90)_6]$ and had dimensions of 300 mm x 300 mm.

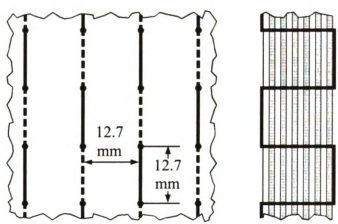

Figure 2-3:Stitching pattern. Top view (a) and cross section (b).

2.2.3 Two-Dimensional Woven Plate

The two-dimensional (2D) woven plate consisted of six pieces of plain weave prepreg that were stacked together. Each piece was very similar to a layer of conventional woven

fabric composite. However, the plies were manufactured from the prepreg tape rather than from a prefabricated woven fabric. Each of the 2D woven pieces had to be woven by hand using a fabricated loom. This process began by cutting the prepreg tape into 458 mm x 12.7 mm strips. The fiber direction was parallel to the cutting direction. The ends of the strips were placed side by side on a warp board, paper backing up, and then secured to the board by masking tape. This procedure was repeated for the other end of the strips, except that a 25 mm length of the paper backing was removed from the end of each strip before taping. Each piece consisted of 26 warp strips. Leaving the paper backing on the strips until it was required to be removed prevented the fibers from getting damaged during the weaving process.

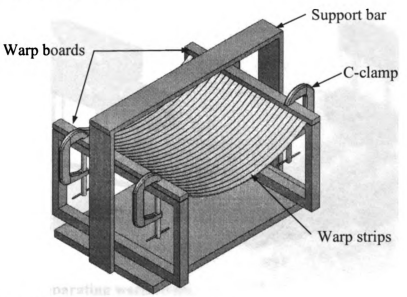

Figure 2-4:Strips attached to stand.

The strips and boards were then attached to a fabricated stand, paper backing down, with c-clamps as shown in Figure 2-4. The warp boards were placed 380 mm apart which created slack in the strips so that they could be moved in the vertical direction when inserting the fill strips. Heddles were fabricated by bending 18 gauge steel wire into the required shape. The heddles were designed so that the warp strips could be

inserted through them after they were fixed at both ends. Two heddle bars, each with thirteen heddles, were used to weave the prepreg strips. The heddles were used to separate the warp strips so that the fill strips could be inserted as shown in Figures 2-5a and 2-5b. One set of heddles would pull up on the even numbered strips while the other set would push down on the odd numbered strips as shown in Figure 2-5a. The heddle bar positions were reversed prior to the next fill strip insertion as shown in Figure 2-5b. The heddle bar in the up position would be clamped to the support bar during fill strip insertion. The weight of the heddle bar in the down position was sufficient to hold the strips in their required position. Approximately 25 mm of paper backing was removed from each warp strip prior to the placement of each fill strip.

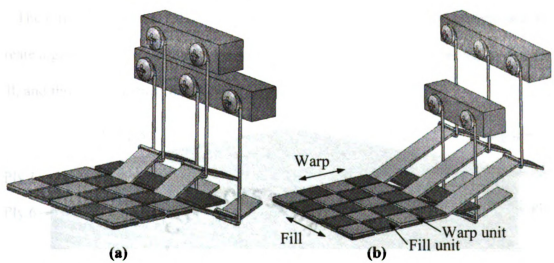

Figure 2-5: Heddles separating warp strips.

The process of switching the heddles, removing paper backing, and placing fill strips was repeated until each piece was completed. Six pieces were individually woven in total and stacked together with both warp and fill units well aligned through the thickness. The 2D woven plates with the geometry shown in Figure 2-6 were designated as 2D[$(\underline{0/90})_6$], where the underline emphasized woven. The panels had dimensions of

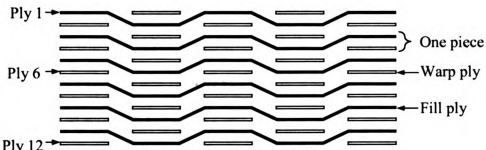

Figure 2-6:Side view of 2D geometry.

300 mm x 300 mm after removing the excessive warp and fill units from all edges. Though not exact, the 2D woven composite plate was close to being symmetric about its midplane. An optical microscope image of the cross section of a portion of a 2D[$(\underline{0/90})_6$] specimen at a magnification of 120X is shown in Appendix A.

2.2.4 Three-Dimensional Woven Plates

The three-dimensional (3D) woven plates used a novel manufacturing technique to create a geometry in which 12.7 mm wide strips of prepreg were interwoven in the warp, fill, and through thickness directions as shown in Figure 2-7.

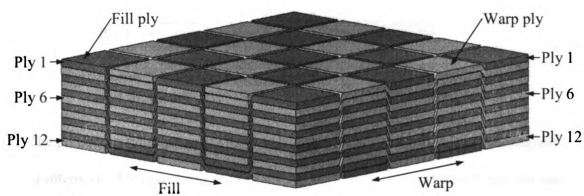

Figure 2-7:3D geometry.

The geometry was similar to the 2D woven plate; however, each ply of the 3D plate was interwoven with the others. The 2D plate consisted of six pieces of plain-woven prepreg that were joined by the epoxy matrix between them. Figure 2-6 shows that in the 2D plate plies 1 and 2, 3 and 4, 5 and 6, 7 and 8, 9 and 10, and 11 and 12 were woven

together. The 3D plate differs because in the warp direction plies 1 and 2, 2 and 4, 4 and 6, 6 and 8, 8 and 10, and 10 and 12 were interwoven together as shown if Figures 2-7 and 2-8a. Plies 1 and 3, 3 and 5, 5 and 7, 7 and 9, 9 and 11, and 11 and 12 were interwoven in the fill direction as shown in Figures 2-7 and 2-8b. This 3D geometry created a plate with the same thickness as the 2D plate but without having only the epoxy matrix to connect each layer.

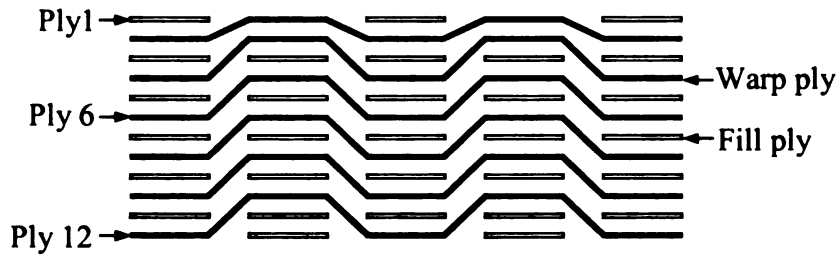

(a) warp direction

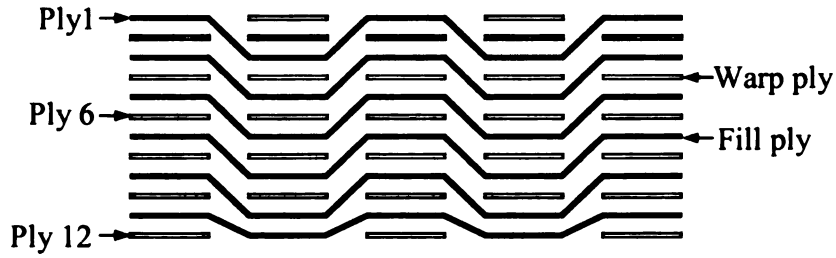

(b) fill direction

Figure 2-8: Three-dimensional weave geometry in warp and fill directions.

The procedure for creating the 3D woven plate was extremely time consuming and labor intensive. This geometry required that each fill row be completed before the next could begin. No automation was incorporated into weaving the plates as no equipment could be found that could create the 3D geometry, thus all weaving was done by hand. All warp strips of the first ply had to be taped, paper backing side up, to a warp board only at one end before weaving could begin. A section of the paper backing was removed from the end of each strip where the tape was placed. The next ply of strips

then had to be placed directly over the previous ply, paper backing removed, and taped to the warp board. This procedure was repeated until all strips of six plies were taped to the warp board. The other ends of the strips were not taped as in the two-dimensional weaving. The fabricated plates consisted of twenty-six strips per ply with the panel having six plies in the warp direction and six plies in the fill direction.

The warp board and strips were secured to an elevated work surface with the paper backing down. Non-perforated Teflon fabric was used to prevent the strips from sticking to the work surface. The 3D weaving process required that warp strips and associated paper backing be folded back in the sequence presented in Figure 2-9. The paper backing remained on the warp strips until they were folded back. The length of paper backing removed depended on the fill angle, but enough length had to be removed so that none remained between the warp strips and fill strips during the weaving of each row. Figure 2-10 shows step 3 prior to placing a fill strip over the warp strips for the 3D[$(\underline{0/90})_6$] plate. The fill strips are folded back and the paper backing has been trimmed.

3D woven plates had orthogonal as well as non-orthogonal angles between warp and fill strips. The fill strips were placed at angles of 15, 30, 45, and 90 degrees from the warp strip direction. These plates were designated as 3D[$(\underline{0/15})_6$], 3D[$(\underline{0/30})_6$], 3D[$(\underline{0/45})_6$], and 3D[$(\underline{0/90})_6$]. The plates had dimensions of 300 mm x 300 mm after the edges were trimmed. An optical microscope image of the cross section of a portion of a 3D[$(\underline{0/90})_6$] specimen at a magnification of 120X is shown in Appendix A.

The procedure for weaving the next fill row followed the same steps. However, the warp strips that were folded back and then placed over the fill strips would change. For example, in step one, the warp strips in rows 1, 3, and 5 would be folded back and all but

one strip in rows 2 and 4 would be folded back. The completed second fill row should look like that given in Step 8 of Figure 2-9. The remaining odd fill rows should be the same as the first fill row while the remaining even fill rows will be the same as the second fill row.

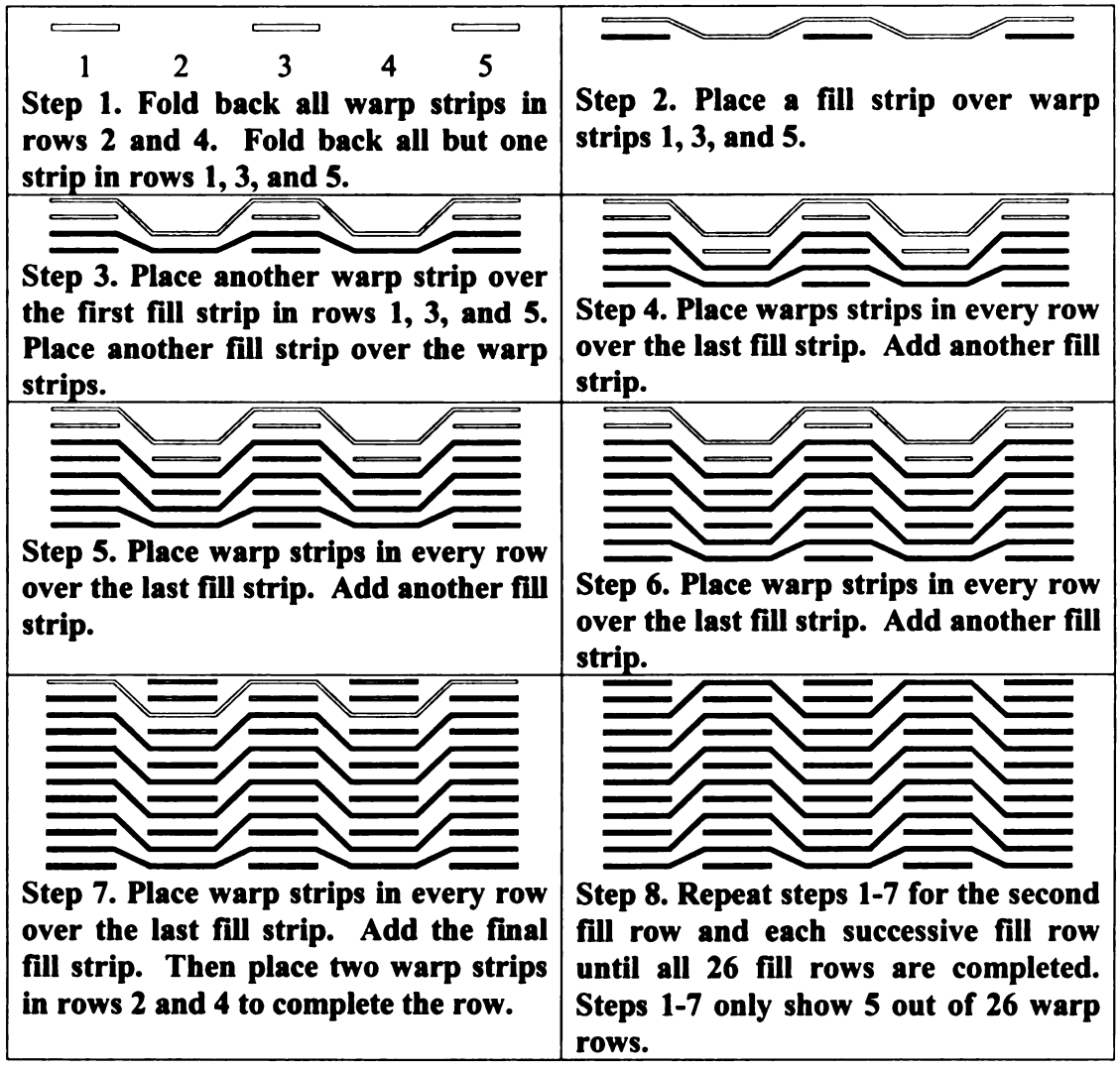

Figure 2-9: Weaving instructions for one row of 3D geometry.

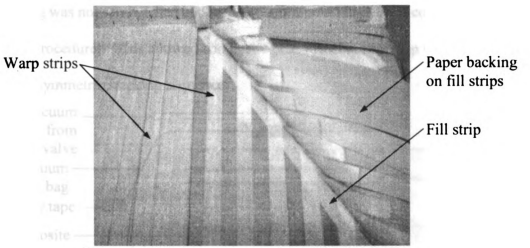

Figure 2-10: Step 3 of weaving 3D[(0/30)$_6$] plate.

2.3 Curing

The composite plates were cured in an autoclave. Six panels were cured at a time to ensure that they all received the same cure cycle. The following cure cycle was used:

1. Set pressure in autoclave to 560 kPa.
2. Ramp temperature from room temperature to 160° C at ten degrees per minute.
3. Hold temperature at 160° C and pressure at 560 kPa for 45 minutes.
4. Cool from 160° C to room temperature at 10° per minute then release pressure.

Vacuum bags were used during the cure cycle along with a vacuum pump to remove air bubbles that formed during curing. The vacuum hoses were attached to vac valves that allowed gases to be removed from the vacuum bags while maintaining negative pressure in the vacuum bags. The vacuum was maintained at 13 inches of mercury (44 kPa) from the beginning of the cure cycle until five minutes into step 3 at which time the vacuum was vented to the atmosphere. Porous Teflon and bleeder fabric was placed on the tops and bottoms of the composite plates as shown in Figure 2-11. Vacuum bags, which were used to contain the composite plates, porous Teflon, and bleeder fabric, were then placed on top of aluminum caul plates. Only one caul plate was used, i.e. the

vacuum bag was not sandwiched between two aluminum plates as in conventional autoclave procedures. This allowed composite plates freedom to warp which was caused by their unsymmetric stacking sequences.

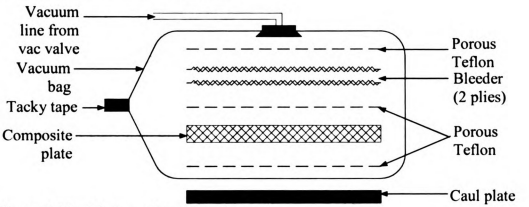

Figure 2-11: Vacuum bagging schematic.

The vacuum line into the autoclave was split into three lines using a manifold constructed of brass tubing and "T" fittings. Each vacuum bag contained two composite plates and one vac valve. The three vacuum lines were attached to the three vac valves. The vacuum bags were separated in the autoclave by fabricated steel stand-offs as shown in Figure 2-12. The middle and upper caul plates and the specimens were not shown.

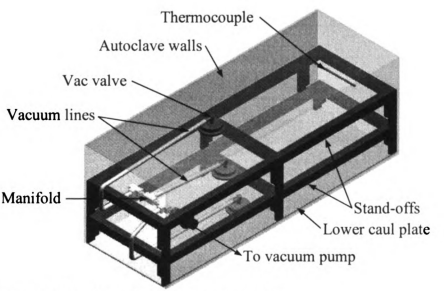

Figure 2-12: Autoclave set-up schematic.

2.4 Specifications

All of the composite plates warped slightly at their corners. This was partially caused by the asymmetry of the plates. The vacuum bags also caused some of the warping. The bags would distort when air was removed from them. The composite plates would conform to the shape of the vacuum bags and cure with the distorted shape. The $L[(0/7.5)_6]$ plate was also slightly deformed by the vac valve during the cure cycle by conforming to the pattern on the bottom of the vac valve. The curved corners of the specimens were removed by a belt sander.

The thickness of each specimen was measured and the average values were recorded in Table 2-1. All specimens had similar thicknesses, as they were all 12 plies thick. The woven specimens were approximately 0.1 mm thicker because of the resin pockets due to the geometry.

Table 2-1: Average thickness of composite plates.

Type	$L[(0/7.5)_6]$	$L[(0/15)_6]$	$L[(0/30)_6]$	$L[(0/45)_6]$	$L[(0/90)_6]$	$S[(0/90)_6]$
Thickness (mm)	2.6	2.6	2.6	2.6	2.6	2.6
Type	$2D[(\underline{0/90})_6]$	$3D[(\underline{0/15})_6]$	$3D[(\underline{0/30})_6]$	$3D[(\underline{0/45})_6]$	$3D[(\underline{0/90})_6]$	
Thickness (mm)	2.7	2.7	2.7	2.7	2.7	

3. Testing

3.1 Testing Facility

The composite plates were tested with an instrumented drop-weight impact tester. Each 300 mm x 300 mm plate was cut into nine 100 mm x 100 mm specimens with a diamond blade circular saw. The drop weight tester consisted of the items labeled in Figure 3-1. The hemispheric nose, 12.7 mm diameter tup was connected to a 22,241 N load cell that was attached to the crosshead. The tup had an overall length of 50.8 mm and a mass of 92.4 g. The crosshead was secured to the height adjustment clamp by a latch. The crosshead and height adjustment clamp could slide with negligible friction along the guide rails. The total weight of the crosshead, load cell, and tup was 49.3 N, which corresponded to a mass of 5.03 kg.

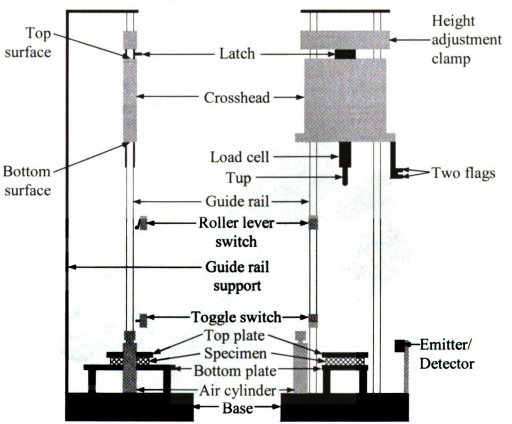

Figure 3-1: Schematic diagram of impact testing machine.

The rebound arrestor consisted of a pneumatic air cylinder, a solenoid valve, relay, a toggle switch, and a roller lever switch as shown in Figures 3-2 and 3-3. The switches were held in place by a stand not shown in the figures. The top and bottom plates of the specimen clamping fixture had cutouts of 76 mm x 76 mm. Four toggle clamps, shown in Figure 3-3, were used to secure the top plate and the specimen to the bottom plate. Toggle clamps were used to ensure that the clamping points and clamping forces were consistent for all types of specimens tested. Clamping resulted in a fixed boundary condition simulating that the specimens were small sections of large structures.

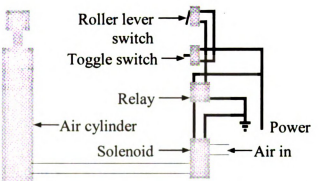

Figure 3-2:Schematic diagram of rebound arrestor.

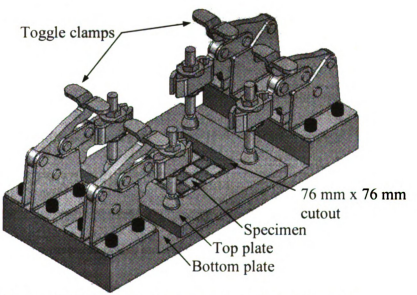

Figure 3-3:Schematic diagram of specimen clamping fixture.

3.2 Operating Procedures

Each test consisted of placing a 100 mm x 100 mm specimen on the bottom plate of the clamping fixture. The top plate was then placed over the specimen and secured with the toggle clamps. The crosshead was then raised to a desired height above the specimen by adjusting the position of the height adjustment clamp. Finally, the latch was pressed to release the crosshead. The crosshead would drop under the force of gravity and be guided by the rails. The tup would strike the specimens at their centers. The centers of the stitched and woven composites were carefully adjusted to be the centers of their unit cells, shown in Figure 3-4. This resulted in the best condition for impact.

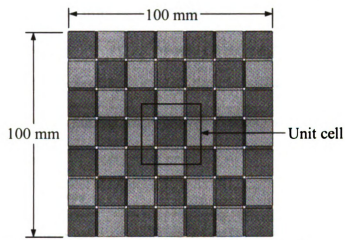

Figure 3-4: Specimen dimensions and unit cell.

A photogate system consisting of the two flags and an infrared emitter/detector was used to determine the impact velocity, v_i. The signal normally read by the computer was zero volts. The flags, shown in Figure 3-1, would produce two five-volt spikes in the signal as they passed through the emitter/detector. Each flag would produce its own individual spike. The data acquisition software would then measure the time between the two spikes. This time, t, and the distance, d (10.3 mm), between the two flags could be

used to determine the impact velocity, i.e. $v_i = d/t$. Both flags needed to be just below the emitter/detector when the tup made contact with the specimens for the computer to be triggered correctly.

The crosshead would move past the roller lever switch then the bottom surface of the crosshead would move the toggle switch to the "on" position while dropping by striking the toggle. This would cause power to be sent to the roller lever switch. In the event of the tup rebounding, the roller lever switch would be hit by the top surface of the crosshead. Since the roller lever switch would have power when the crosshead hit it the second time, the relay would latch and open the solenoid valve causing the air cylinder to extend thus preventing the tup from hitting the specimen a second time. The toggle switch was positioned so that it would be turned "on" just as the tup made contact with the specimens. The roller lever switch was located 270 mm above the toggle switch for all tests. The load on the tup during impact was recorded by a computer and subsequent data analysis was performed by a computer program.

3.3 Load-Deflection Curves

The composite specimens were tested by adjusting the drop height while keeping the crosshead weight constant. Tup load, *F(t)*, was recorded at a sampling rate of 25 μs which was used to calculate the acceleration, *a(t)*, after dividing by the combined mass, *m*, of the crosshead, load cell, and tup, i.e.

$$a(t) = F(t)/m. \tag{3.1}$$

Throughout this thesis, *m* was equal to 5.03 kg for all tests. The computer would record 2048 data points during each test resulting in the maximum capability of recording an impact event of 50 ms. This duration was sufficient for all of the impact tests performed

in this thesis. The velocity, *v(t)*, at each time step was calculated by integrating the acceleration, *a(t)*, using Equation (3.2) where 0 corresponded to the time when the computer began recording load data, *t* was the duration of the event, and v_i was the impact velocity measured by the photogate system.

$$v(t) = -\int_0^t a(t)dt + v_i \tag{3.2}$$

The deflection history, $\delta(t)$, was calculated by integrating the velocity history using Equation (3.3).

$$\delta(t) = \int_0^t v(t)dt \tag{3.3}$$

Since both load and deflection could be expressed as functions of time, the direct relation between load and deflection, i.e. the load deflection relation

$$F = f(\delta) \tag{3.4}$$

could be established. The load-deflection curve was then used to determine the absorbed energy, E_a, using Equation (3.5) where δ_t was the deflection when the force became zero again at the end of impact.

$$E_a = \int_0^{\delta_t} F(\delta)d\delta \tag{3.5}$$

A program was written in MATLAB to perform the calculations listed in the above equations and is included in Appendix B.

3.4 Discussion

The tup was made of high carbon steel and subjected to heat treatment. It was assumed to be perfectly rigid for all tests conducted. The load applied to the tup was transferred to the load cell that was not perfectly rigid. The load cell would deform and the deformation would be measured by four strain gages attached to the load cell. The purpose of using four strain gages on a square load cell was to compensate for the effect due to bending. The strain measurement would then be multiplied by a calibration factor of 3326 to calculate the load. The calibration factor was determined by calibrating the load cell using quasi-static compression. The calibration curve for the 22,241 N load cell is shown in Appendix C. The assumption of perfect rigidity and the mass (92.4 g) of the tup in front of the load cell, along with the accuracy of the calibration factor, could cause some errors to the measurement of the tup load, $F(t)$. These errors should be included in the ultimate analysis of experimental accuracy.

4. Data Analysis

4.1 Energy Profile

The objective of this thesis research was to determine the energy levels required to cause penetration and perforation of composite plates, the so-called penetration and perforation thresholds. A method based on impact and absorbed energies was used for determining the thresholds [17]. This method was called the energy profiling method. A sketch of a typical energy profile for specimens subjected to central impact is given in Figure 4-1. The solid circles resemble experimental results. They are based on the energy delivered to the specimens, i.e. the impact energy, E_i, and the energy absorbed by the specimens, i.e. the absorbed energy, E_a. The impact energy values included both kinetic energy and potential energy. The absorbed energy values assumed all forms of energy absorption, such as elastic and plastic deformation, fracture, and friction. There was also energy absorbed by the testing facility in terms of vibration and heat. Hence, the absorbed energy values were usually less than their respective impact energies for specimens subjected to central impact.

Figure 4-1 shows that the absorbed energy increases as the impact energy increases. There comes a point where the impact energy and the absorbed energy first become equal to each other. This point is called the penetration point and the corresponding energy value, the penetration threshold. As the impact energy further increases, the impact and the absorbed energies remain equal to each other, namely, the equal energy interval. It is also called the penetration process zone. There comes another point just before the impact energy becomes greater than the absorbed energy again. This point is called the perforation point and the corresponding energy value, the perforation threshold.

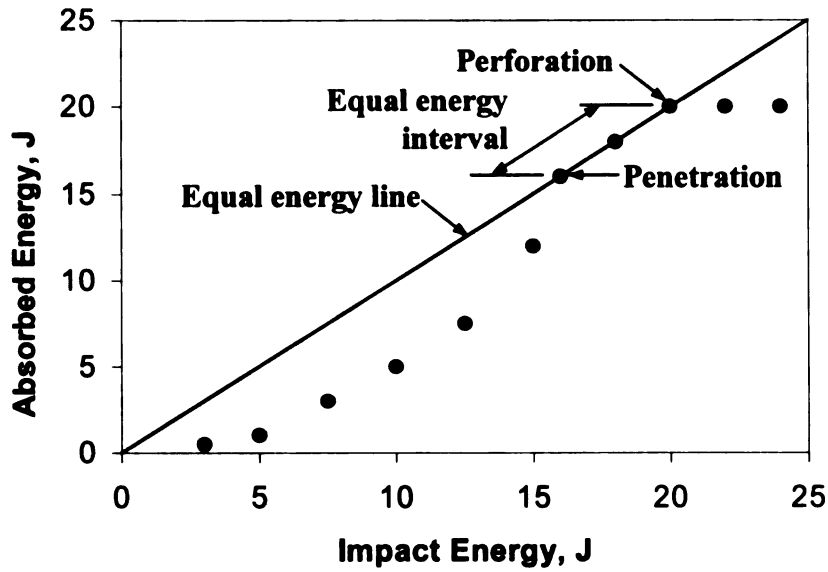

Figure 4-1: Energy profiling method for determining penetration and perforation.

4.2 Test Specimens

The first group of tests conducted was on a polymeric material reinforced with short glass fibers in random orientations. The specimens were impacted and the energy profile was established. This study was performed so that the user could become familiar with the instrumented drop-weight impact tester, rebound arrestor, data acquisition, data processing, and the energy profile method. It was also performed to establish the protocols of experiment and data analysis that would be used later for the glass/epoxy composite plates.

The load-deflection curves of the test specimens are shown in Figure 4-2. The curves were established from data calculated by the software prepared by the manufacturer of the instrumented drop-weight impact tester. Figure 4-2 shows that the specimens tested produced open and closed curves. It is also noted from the figure that the eleven curves overlap well in both the loading and unloading sections although the discrepancy on the peak load seems to be significant. The closed curves, numbered 1, 2, and 3, are for

specimens that experienced rebounding of the tup from the specimens, while the open curves, numbered 4-11, are for specimens that experienced penetration of the tup into or perforation of the tup through the specimens. Penetration was defined as the first instant the tup did not rebound from a specimen. Perforation, however, was defined as the instant when the tip of the tup just broke through the backside of the specimens being tested.

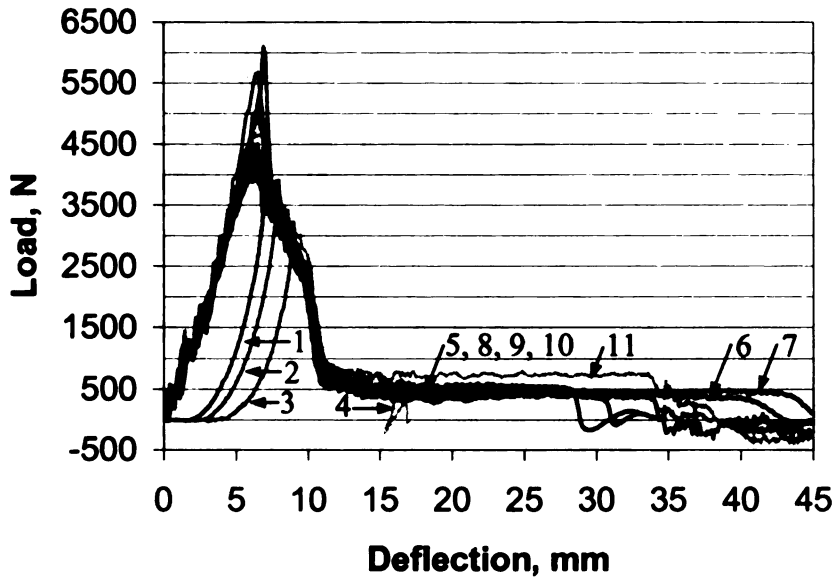

Figure 4-2: Load-deflection curves of test specimens.

Figure 4-3 shows the energy profile for the eleven curves given in Figure 4-2. The impact and absorbed energies used in generating the energy profile are based on the values calculated by the manufacturer's software. Data points 1, 2, and 3 had impact energies smaller than the corresponding absorbed energies as the tup rebounded during these impact tests. Data points 4-8 were located above the equal energy line, indicating that they absorbed more energy than what was inputted to them. Data points 9 and 11 appeared to be very close to the equal energy line. Inspections of the specimens revealed that specimens 4 through 11 had been perforated. The absurdity of the results that the absorbed energy was greater than the impact energy required more careful analysis.

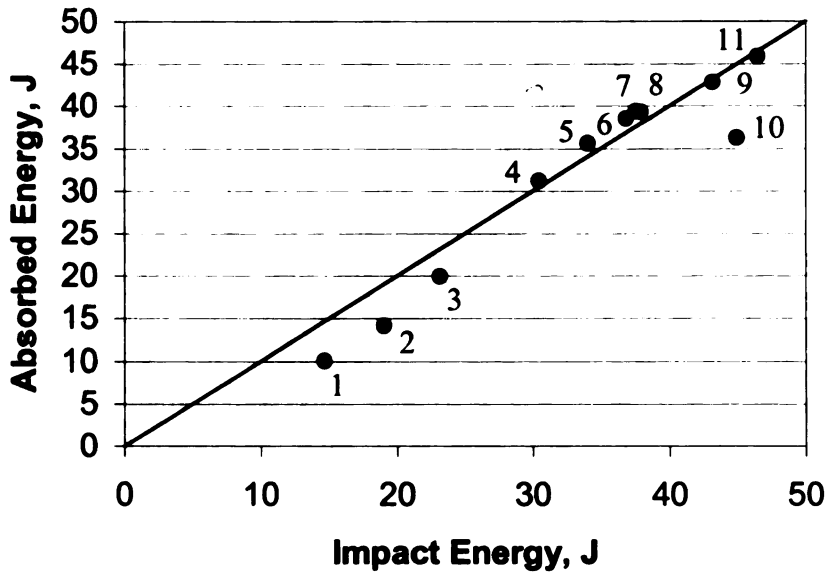

Figure 4-3: Energy profile of test specimens.

4.3 Frictional Effect

Friction played an important role in the impact study. Six additional test specimens were impacted to study the frictional effect. These specimens were made of the same materials as those tested previously. Three specimens received no lubrication prior to impact, while the other three were lubricated with a 6% silicone mold release product. The silicone was spread on the surface of the specimens at the point where the tup would impact them. The tup was lubricated with silicone as well. Table 4-1 gives the results of the lubrication test. The impact energies and absorbed energies were obtained from the manufacturer's software while the corrected energies and extended method energies were based on methods presented in later sections.

Table 4-1: Results of friction effect tests.

		Software Results		Velocity Based Correction Method		Extended Method	
Test	Lubricant	E_i (J)	E_a (J)	E_i (J)	E_a (J)	E_i (J)	E_a (J)
1	No	34.46	35.18	34.80	29.45	35.29	27.97
2	No	34.49	32.73	34.83	26.55	35.32	25.24
3	No	34.29	35.64	34.61	26.36	35.13	25.26
4	Yes	34.52	29.75	34.82	25.81	35.32	25.32
5	Yes	34.53	28.89	34.85	25.03	35.31	23.93
6	Yes	34.48	31.08	34.79	26.83	35.27	25.89

Lubricating the top surfaces of the specimens and the tup did reduce the absorbed energy. This was a result of decreasing the friction between the specimens and the sides of the tup. Less friction resulted in the load cell recording less load on the tup, thus less area enclosed by the load-deflection curves as shown in Figure 4-4. The load-deflection curves are all very similar up to the point where the load became nearly constant. Specimens 4, 5, and 6 have lower constant load values after that point.

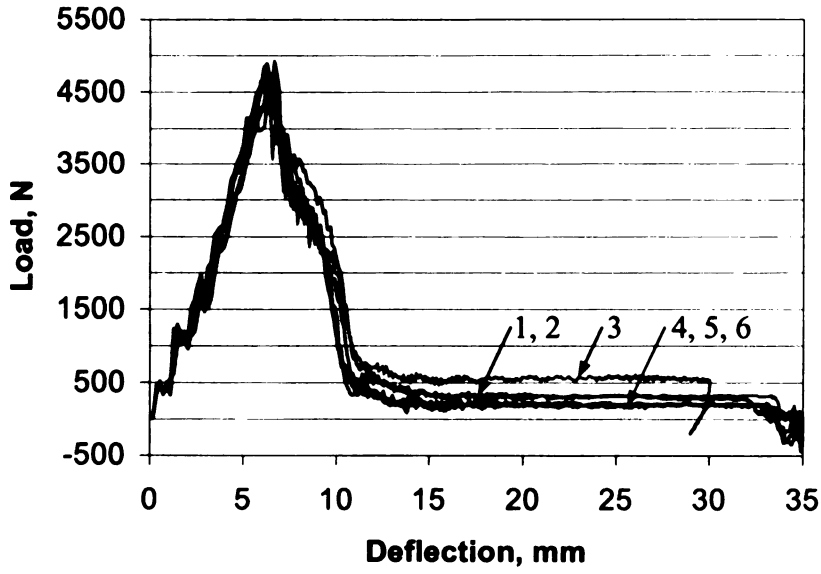

Figure 4-4: Load-deflection curves of lubrication test.

4.4 Measurement of Perforation Depth

The deflection values used to generate the load-deflection curves, like those in Figure 4-4, were based on the calculations mentioned earlier. The deflection values were checked by placing soft green craft foam 12.7 mm below the test specimens so that it would not interfere with the deflection. The foam had a density of .0328 g/cm^3. The crosshead was then dropped from various heights. The tup perforated the test specimens and penetrated into the foam. The value, D_M, was the distance measured from the end of the tup to the top of the undeformed specimen. The depth of the tup penetration into the foam, D_E, was also measured. The perforation depth, DP, was calculated by Equation (4.1) where 50.8 was the length, in millimeters, of the tup and D_M was the measured distance. The value of DP indicated how far the tip of the tup moved below the top of the specimen during the impact event.

$$DP = 50.8 - D_M \tag{4.1}$$

D_C was the value given by the manufacturer's software for how far the tip of the tup moved below the top of the specimen during the impact event. D_E was used to verify the values of DP. This could be done by using Equation (4.2) where 12.7 (mm) was the distance from the bottom of the specimen to the top of the foam and h was the thickness of the test specimens. The test specimens were 3 mm thick. The values calculated by Equation (4.2) were labeled DP^*.

$$DP^* = D_E + 12.7 + h \tag{4.2}$$

Table 4-2 gives the values for the dimensions shown in Figure 4-5. Tests 1-4 had the tup travel through the specimens less than what the manufacturer's software calculated.

Test 5 showed the calculated perforation to be less than the actual perforation. The values of D_C and D_P should have been equal. These tests indicate a large discrepancy between the measurements based on the manufacturer's software and the soft green foam. The D_P and D_P^* values were similar if not identical. This indicated that this method for measuring penetration depth was accurate. The slight discrepancies were due to measurement errors of the D_E values. Friction occurred between the tup and the specimens after penetration; however, there was also slippage. The slippage was most likely the reason for the discrepancies between the D_C and D_P values. Further investigations were deemed necessary.

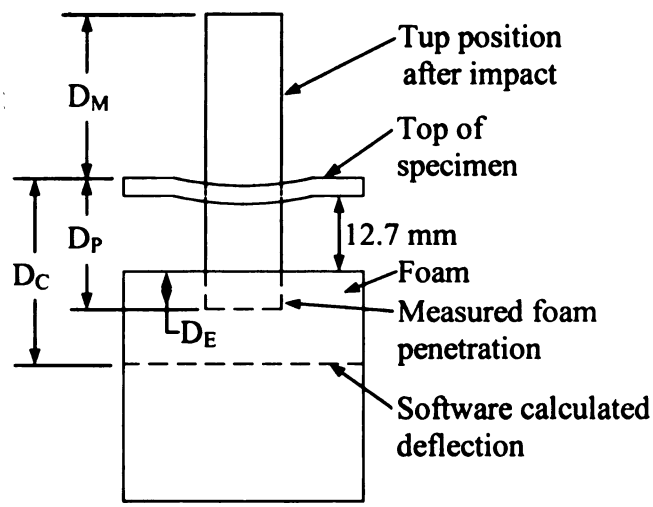

Figure 4-5: Dimensions and notations for tup perforation tests.

Table 4-2: Results of perforation depth tests.

Test	Impact Height (mm)	D_E (mm)	D_M (mm)	D_C (mm)	D_P (mm)	D^*_P (mm)	$D_C - D_P$ (mm)
1	838.2	6.4	27.0	31.2	22.1	22.1	9.1
2	1066.8	22.2	11.1	46.0	38.1	37.9	7.9
3	965.2	15.9	16.7	45.5	32.5	31.6	13.0
4	965.2	4.8	27.8	45.2	20.6	20.5	24.6
5	965.2	10.3	22.2	9.7	26.2	26.0	-16.5

The foam did not affect the results as indicated by the load-deflection curves of Figure 4-6. Both tests were conducted using the same drop height, *h*, value. The load-deflection curves are nearly identical with similar peak load values and a constant load value of about 500 N beginning at a deflection of approximately 12 mm.

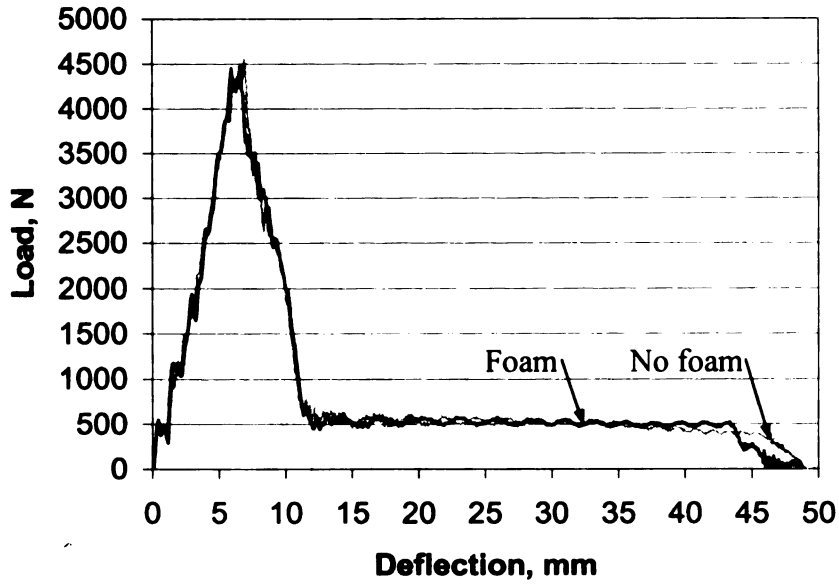

Figure 4-6: Load-deflection curves with and without foam.

4.5 Data Recording

The tup first impacted the specimens with its hemispheric nose. The recording of the load data was started by the flag passing through the emitter/detector. The load data was recorded continually as the tup advanced into the specimens. The recording of the load data was terminated when the load became zero or negative. The load value was not zero when perforation took place for the specimens tested. This was attributed to the sides of the tup rubbing on the specimens and the induced shear loads developing into normal loads at the load cell. Since the data recording unit did not know when the tup perforated the specimens it kept recording load data even when the load was caused by the sides of the tup rubbing on the specimens. This caused the time of the impact event to be much

longer than it took the tup to perforate the specimens. Consequently, the area under the load-deflection curves was increased. When the load was integrated with respect to deflection, excessive absorbed energies were calculated which did not correctly portray the behavior of the impacted specimens. The specimens would seem more resistant to perforation than what they really were. The excessive recording of load data and the friction slippage beyond the penetration point required special attention in the data analysis.

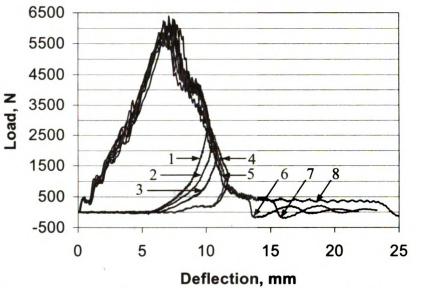

Figure 4-7: Load-deflection curves of L[(0/90)$_6$] specimens.

4.6 Load-Deflection Curves for L[(0/90)$_6$]

Figure 4-7 shows eight load-deflection curves of the L[(0/90)$_6$] specimens. They all have a mountain-like shape indicating a significant strain softening after the peak force. The loading sections are slightly concave due to the in-plane constraint caused by the fixed boundary condition. The eight loading sections seem to overlap up to some extent and the values of the eight peak forces are very similar. The unloading sections also overlap well. The overlapping and similarities of the curves indicate the consistency of

material properties and testing conditions among the eight specimens. Rebounding resulted in closed curves while penetration and perforation produced open curves. The curves of specimens 1-5 have rebounding sections while the remaining curves do not.

Absorbed energies for the specimens with rebounding sections were determined by calculating the areas enclosed by the load-deflection curves. Absorbed energies for the specimens with open curves, such as specimens 6-8, were determined by calculating the area bounded by the load-deflection curves and the horizontal axis, i.e. the deflection axis. The long tail of the open curves indicated an additional absorbed energy from friction between the sides of the tup and the specimens. This friction occurred after the tup perforated the specimens. It maintained a relatively constant energy absorption level.

4.7 Calculations of Energies

Figure 4-8 presents the energy profile of the $L[(0/90)_6]$ specimens with the load-deflection curves given in Figure 4-7. The absorbed energies were based on the area enclosed by the curves or under the curves as mentioned earlier. The impact energies, E_i, were based on the following equation

$$E_i = mgh \tag{4.3}$$

where m was the combined mass of the crosshead, load cell, and tup, g was the gravitational acceleration, and h was the distance between the tip of the tup and the surface of the specimens before the drop tests took place.

The impact energy could also be expressed in terms of kinetic energy instead of potential energy, i.e.

$$E_i = \frac{1}{2} m v_i^2 \tag{4.4}$$

where v_i was the so-called impact velocity measured by the photogate just before the tup impacted the specimens.

The impact velocity values from the photogate could be verified by equating the kinetic energy to the potential energy.

$$v_i = \sqrt{2gh} \tag{4.5}$$

The results from the photogate and Equation (4.5) were very similar and should have been exact if there was no friction between the crosshead and guide rails.

Three of the ten points corresponding to specimens 6, 7, and 8 had absorbed energy values greater than their respective impact energies. Apparently, the calculations of the energies were not correct and required more careful analysis.

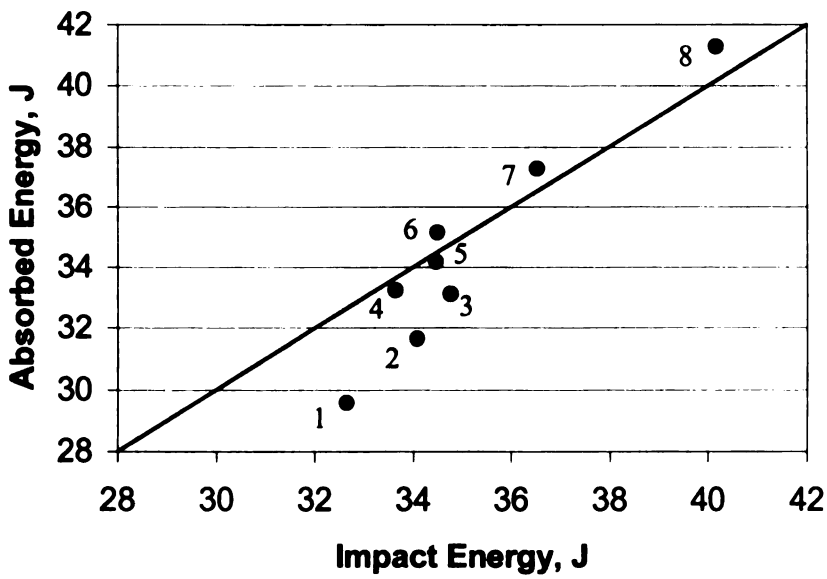

Figure 4-8: Energy profile of L[(0/90)$_6$] specimens.

The absorbed energies calculated from integrating the load-deflection curves, as mentioned earlier, covered the entire load-deflection curves. More specifically, they included the period of friction between the tup and the specimens after the composite plates were completely perforated. Accordingly, the absorbed energies calculated by the

integration of the entire load-deflection curves did not really reflect the energy absorption capability of the composite plates. They were higher than the composite plates could take. The calculation of the energy absorption capability would be correct if the load-deflection curves ended at the perforation points, instead of at the ends of the impact events.

4.8 Correction of Energy Calculations

4.8.1 Correction of Absorbed Energy

Based on the forgoing discussion, a method was developed to correct the values of the absorbed energy given by the manufacture. This method utilized the perforation point as the ending point of energy integration and was useful for the specimens with open load-deflection curves. However, this method did not apply to the specimens with closed load-deflection curves because there was no friction between the tup and the specimens due to the rebounding process.

The goal of the drop weight testing was to determine the amount of the energy that each specimen could absorb up to perforation. The corresponding velocity-deflection curve was used to determine the perforation point. The reason was that the velocity-deflection curves leveled off once perforation occurred due to the steady process of friction, i.e. no further damage process in the composite plates. Figure 4-9 presents the load-deflection curve and the corresponding velocity-deflection curve of L[$(0/90)_6$] specimen 8.

The load value in Figure 4-9 increased quickly, reached a peak value of 5923 N, and then decreased sharply. The load value then leveled off and became nearly a constant value of 400 N. Friction between the sides of the tup and the specimen started when the

load became nearly constant. The point where the load became constant was deemed the perforation point.

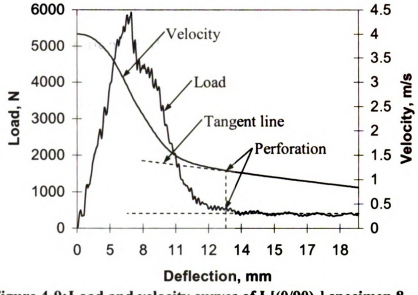

Figure 4-9: Load and velocity curves of L[(0/90)$_6$] specimen 8.

The velocity curve began with a value of 4 m/s which corresponded to the impact velocity. The velocity decreased as the tup was in contact with the specimen. There was then a bend in the curve as the load approached the peak value and then the velocity decreased at a constant rate along the unloading section of the load-deflection curve. Another bend occurred in the velocity near the end of unloading. The velocity decreased constantly again after that point. The starting point of the second constant decrease in velocity was indicative of the starting point of constant friction between the sides of the tup and the specimen. Thus, the constant decrease in velocity began when the tup perforated the specimens. A tangent line with respect to the velocity-deflection curve was drawn to identify the perforation point as shown in Figure 4-9. Another fitting line was drawn on the load-deflection curve, also shown in Figure 4-9. The perforation points determined by the load and velocity curves agreed were very close.

This method of determining the perforation points was similar to that used by Baucom and Zikry [18]. In their study, the specimens were deemed perforated when the tup displacement reached a value that was equal to the sum of the specimen thickness and the diameter of the hemispheric nose. However, their impact testing was conducted under quasi-static loading rates (10-80 μm/s). They also observed a point where the load became a nearly constant value.

Based on the perforation points determined from the velocity-deflection curves, the absorbed energy values that matched the deflection values at perforation were used as the corrected absorbed energies. This method of correcting the absorbed energy was subsequently used for all specimens that were perforated.

4.8.2 Correction of Impact Energy

The original method used Equation (4.3) or Equation (4.4) to calculate the impact energy. This method did not take into account the energy introduced to a specimen by the crosshead, load cell, and tup during the impact, i.e. from the contact impact until the end of the impact event. This additional impact energy could be characterized as potential energy in the following equation.

$$E_i^a = mgh' \tag{4.6}$$

This additional energy had to be added to the impact energy calculated by Equations (4.3) or (4.4) in order to have the correct impact energy.

The value of h' was the tup deflection beyond the top surface of the specimen after the initial contact took place. The method for determining h' was dependent on whether the tup rebounded or perforated the specimens. The maximum deflections calculated by Equation (3.3) were used if the tup rebounded from the specimens. The deflection values

corresponding to the perforation points found from curves like those presented in Figure 4-9 were used if the tup perforated the specimens.

Equations (4.3) and (4.6) could be combined into Equation (4.7) to calculate the corrected impact energy.

$$\begin{aligned} E_i^C &= mgh + mgh' \\ &= mg(h + h') \end{aligned} \tag{4.7}$$

Eliminating the absorbed energy due to the post-perforation friction, i.e. the corrected absorbed energy, and calculating the impact energy with Equation (4.7), i.e. the corrected impact energy, gave the energy profile of the L[(0/90)$_6$] shown in Figure 4-10. None of the points are located above the equal energy line. Also, none of the points are located on the equal energy line, which implies that there was energy loss due to heat and vibration during the impact events.

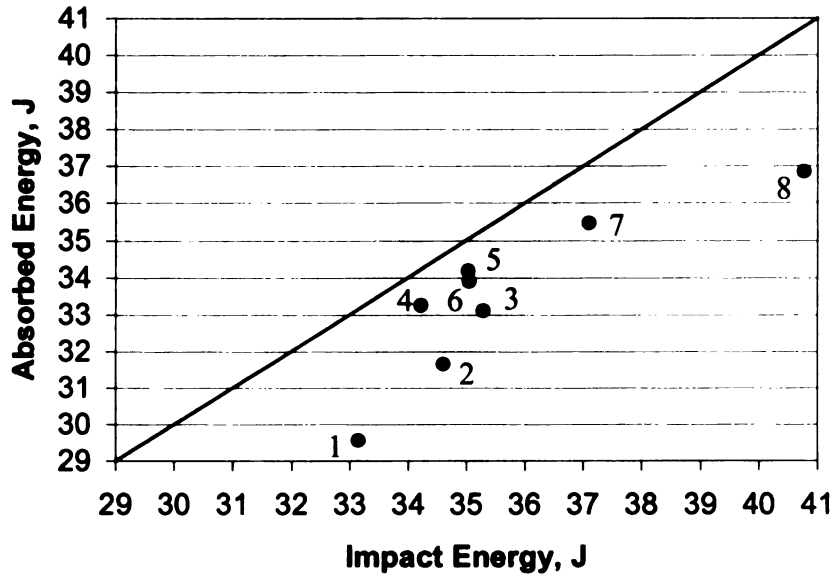

Figure 4-10: Corrected energy profile of L[(0/90)$_6$] specimens.

The corrected method would abruptly end the load-deflection and velocity-deflection curves at the perforation points. The testing showed the loads gradually decreasing to zero after the friction portions of the load-deflection curves. The corrected energy

method did not take into account this small area. This area only accounted for approximately 0.5 J of energy so it was deemed negligible.

4.9 Other Correction Methods

The corrected energy methods for obtaining corrected impact energy and corrected absorbed energy seemed to characterize the energy absorption capabilities of the specimens more accurately than using the method provided by the manufacturer. Other methods were also investigated in attempts to correct the absorbed energies.

4.9.1 Friction Removal Correction Method

The first method used the measured perforation depth and the load-deflection curves to correct the absorbed energy. This method began by testing a specimen with the instrumented drop-weight impact tester. Absorbed energy needed correction only if the tup perforated the specimens. The distance from the end of the tup to the top of the specimens was measured by a ruler after the tup had finished moving through the specimens. This measured distance, D_M, is shown in Figure 4-11. The distance that the tup moved through the specimens while encountering friction between the sides of the tup and specimen could then be calculated by

$$D_F = 46 - D_M \tag{4.8}$$

where 46 was the length, in millimeters, of the side of the tup, and D_F was the friction distance.

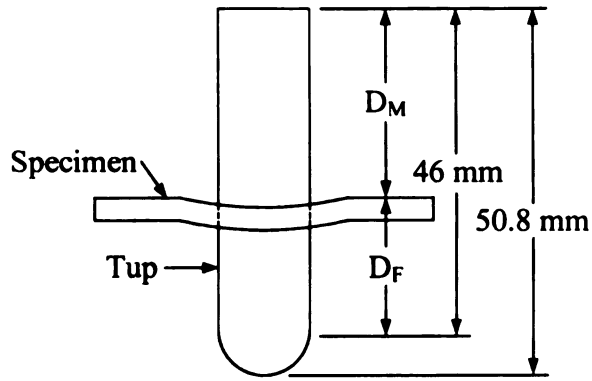

Figure 4-11: Tup measurements made for friction removal correction method.

The friction distance, D_F, was then removed from the tail of the load-deflection curve of each specimen that had been perforated as illustrated in Figure 4-12 for test 6 of the test specimens. The friction distance was 27 mm so the portion of the load-deflection curve between 13 mm and 40 mm was removed. The remaining portions of the curve up to 13 mm and between 40 mm to 43 mm were joined together. The new load-deflection curve, Figure 4-13, could then be used to calculate the absorbed energy. There was a discontinuity in the load at a deflection of 13 mm. This occurred because the load was not equal at deflections of 13 mm and 40 mm.

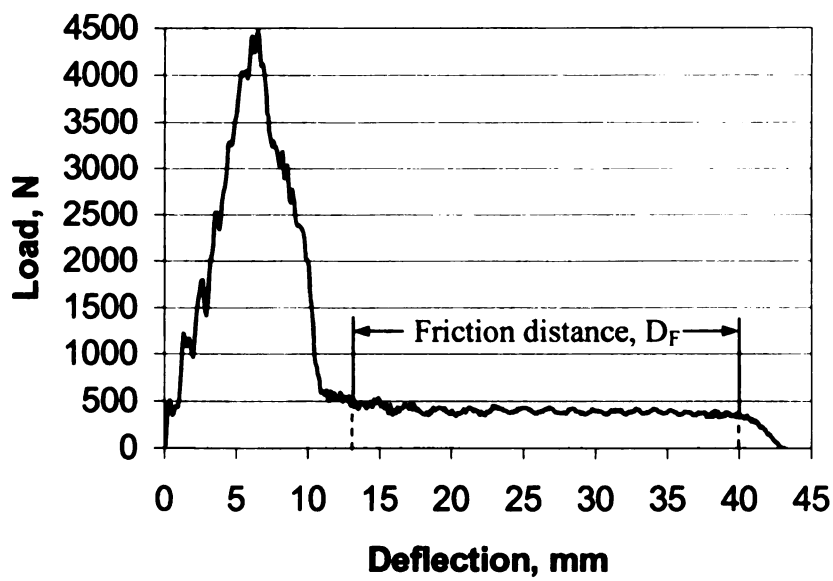

Figure 4-12: Removing friction distance of test specimen 6.

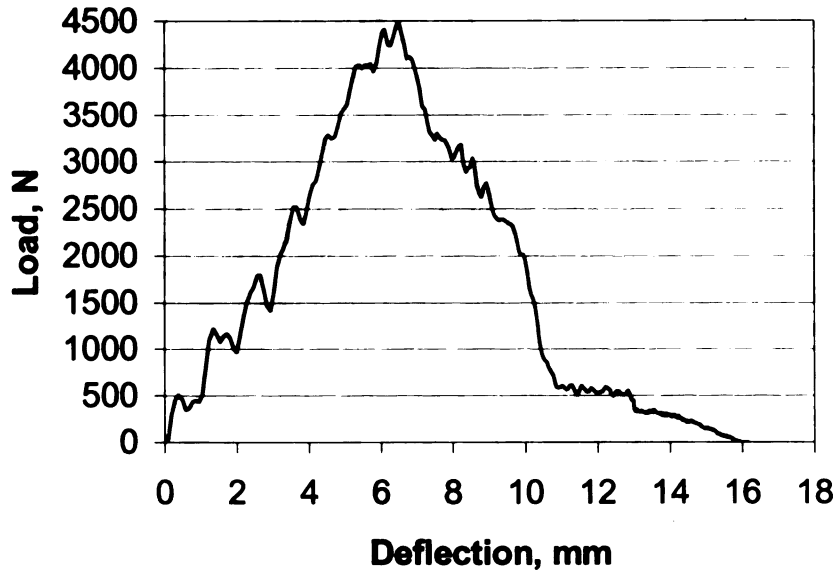

Figure 4-13: Modified load-deflection curve of test specimen 6.

The friction removal correction method was used on test specimens 6 and 7 to correct the absorbed energies and impact energies. Their original load-deflection curves are shown in Figure 4-2. The results for the correction method and friction distance correction method are given in Table 4-3. The impact energies were similar because different *h* ' values were used in the calculations, but the absorbed energies were not. The absorbed energy values are greatly affected by the load-deflection curves. The friction removal correction method was not as accurate as the velocity based correction method because it used the deflection values calculated after perforation, hence the friction portion of the load-deflection curves, where a portion was removed, could have been incorrect. The deflection values were shown to be questionable in Section 4.4.

Some of the tests could not have the friction removal subtraction method used. This was because when the friction distance was subtracted, the load-deflection curves would end in the unloading portions. Friction did not occur during the unloading portions so the load-deflection curves must have been incorrect beyond the perforation point.

Table 4-3: Results of friction removal correction method.

	Velocity Based Correction Method		Friction Removal Correction Method	
Test	E_i (J)	E_a (J)	E_i (J)	E_a (J)
6	37.41	26.64	37.61	27.86
7	38.24	26.87	39.01	32.36

4.9.2 Extended Method

Another way to correct the energy absorbed by the specimens was termed the extended method. This method was based on extending the unloading section (excluding the rebouding part) to the deflection axis for both closed and open load-deflection curves. This method was used as a way to estimate the amount of energy required for perforation. The absorbed energy calculated by the extended method would be larger than the values calculated by the corrected method for specimens that had a rebounding section. The triangle method could be used as a way to predict penetration energy even if the tup rebounded during testing.

The load-deflection curve of the $L[(0/90)_6]$ specimen 4 is presented in Figure 4-14. The tup rebounded from this specimen as is evidenced by the curve being closed. This specimen could have absorbed more energy while being penetrated by the tup. The unloading section of the curve would have continued along its slope and intersected the deflection axis at a point beyond 12 mm if the tup had penetrated the specimen and not rebounded. This extension of the slope is shown by the dashed line. The post-perforation friction would not have occurred because the sides of the tup did not pass through the specimen. The extended load-deflection curve could be used to calculate the absorbed energy for penetration. The impact energy could also be corrected using

Equation (4-5) where *h'* would have been the deflection value at the intersection of the softening curve and the deflection axis as indicated in Figure 4-14. Figure 4-15 illustrates how the extended method would be used for specimens that were perforated. The load recorded due to friction would not be used for calculating absorbed energy.

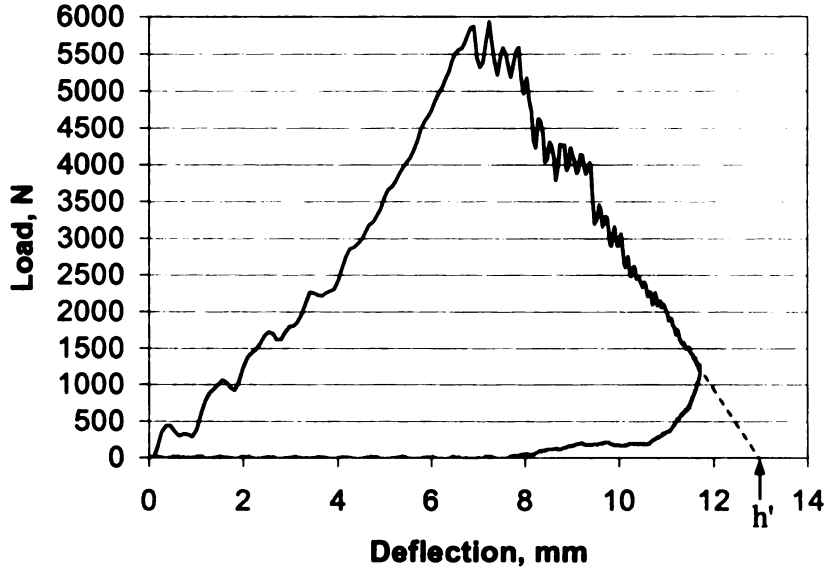

Figure 4-14: Extended method for L[(0/90)$_6$] specimen 4.

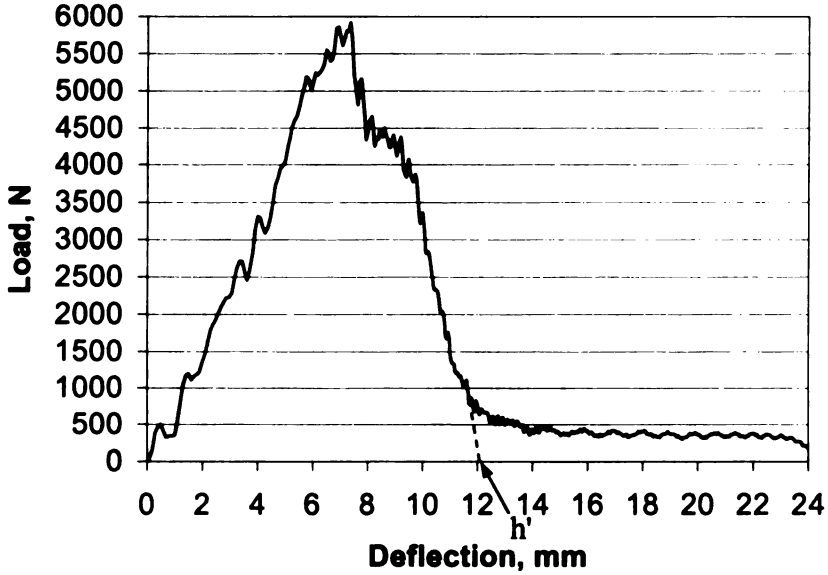

Figure 4-15: Extended method for L[(0/90)$_6$] specimen 8.

This method would not work well if there was not a well defined unloading section of the load-deflection curve. Specimens 1 and 2 of the L[$(0/90)_6$] plate could not be used for the extended method since they did not have well defined unloading sections. Table 4-4 presents the absorbed energies and impact energies of the L[$(0/90)_6$] specimens from the results based on the manufacturer's software, velocity based correction method, and the extended method.

Table 4-4: Comparison of absorbed energy correction methods.

		Software Results			Velocity Based Correction Method				Extended Method		
Specimen	Tup	E_i (J)	E_a (J)	h' (mm)	E_i (J)	E_a (J)	E_i-E_a (J)	h' (mm)	E_i (J)	E_a (J)	h' (mm)
1	Rb	32.65	29.57	10.15	33.15	29.57	3.58	10.15	-	-	-
2	Rb	34.09	31.66	10.46	34.60	31.66	2.94	10.46	-	-	-
3	Rb	34.76	33.11	10.77	35.29	33.11	2.18	10.77	35.32	36.00	11.50
4	Rb	33.64	33.24	11.72	34.22	33.24	0.98	11.72	34.26	34.89	12.80
5	Rb	34.46	34.17	11.47	35.03	34.17	0.86	11.47	35.04	35.23	11.80
6	Pr	34.49	35.16	13.46	35.06	33.90	1.16	11.43	35.07	34.14	11.80
7	Pr	36.53	37.27	15.49	37.10	35.45	1.65	11.68	37.11	35.70	12.20
8	Pr	40.16	41.28	24.38	40.77	36.85	3.92	12.45	40.73	36.10	11.80

The velocity based correction method and the extended method produced similar results. The extended method absorbed energies for tests 3-5 are greater than the velocity based corection method absorbed energies because those tests had rebounding. The extended method shows how much energy may have been required to penetrate but not perforate the specimens for tests 3-5.

Both methods had corrected the impact energy to include the additional energy in the form of mgh'. The h' values for each method were similar as shown in Table 4-4. The velocity based correction method had all absorbed energies less than the impact energies, while the extended method had absorbed energies slightly greater than impact energies for tests 3-5. These tests had rebounding sections so the absorbed energies are an estimate of how much they could have absorbed. Another possible explanation is that the

extended unloading slope could have intercepted the deflection axis at a value greater than it would have in actual testing leading to an overestimate of the absorbed energy.

5. Experimental Results and Discussions

The velocity based correction method was chosen to present the energy data for all of the specimens tested. This method effectively eliminated the absorbed energy resulting from the sides of the tup and specimen interactions. It also gave more representative values for the amount of energy being inputted to each specimen.

The load-deflection curves, energy profiles, and energy values used to characterize some representative samples are given below. The results of other specimens are given in Appendices C-F.

5.1 Load-Deflection Curves and Energy Profiles

5.1.1 Laminated Specimens

Five different laminate configurations were tested. They were designated as $L[(0/\theta)_6]$ with θ being equal to 7.5°, 15°, 30°, 45°, and 90°. The load-deflection curves of the $L[(0/90)_6]$ specimens along with their energy profiles are shown in Figures 5-1 and 5-2, respectively. The load-defection curves and energy profiles for the other laminated

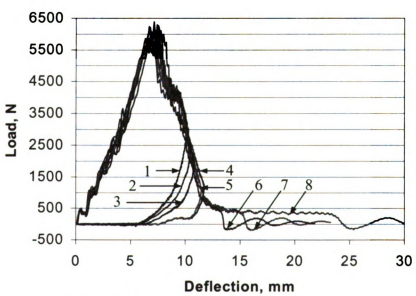

Figure 5-1: Load-deflection curves of $L[(0/90)_6]$ specimens.

specimens, i.e. L[(0/7.5)$_6$], L[(0/15)$_6$], L[(0/30)$_6$], L[(0/45)$_6$], are given in Appendix D.

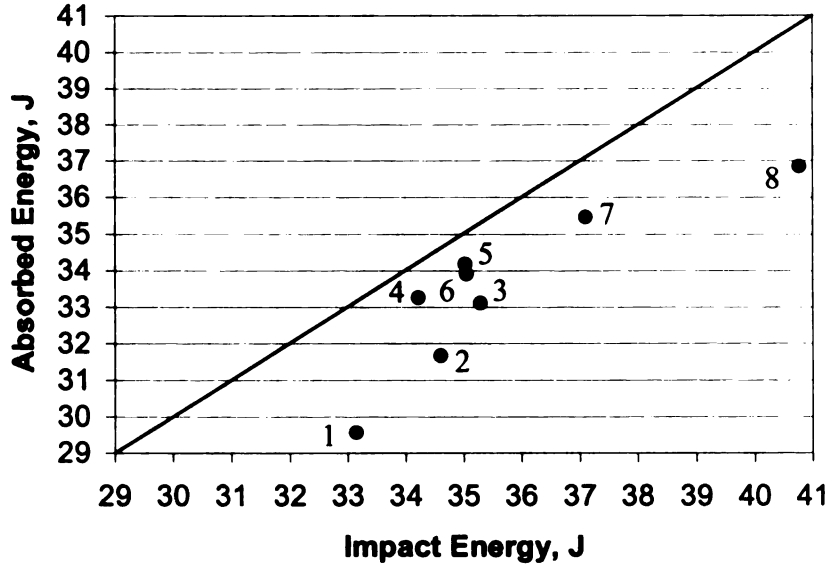

Figure 5-2: Energy profile of L[(0/90)$_6$] specimens.

The load-deflection curves of the specimens tested seem to overlap well in the loading and unloading sections, indicating consistency in both material properties and testing conditions. Specimens 2-6 were chosen to illustrate the penetration and perforation thresholds of the L[(0/90)$_6$] specimens. Specimens 2-5 were chosen because they were almost penetrated by the impact energy inputted to them. Specimen 6 was chosen because its value of impact energy just caused perforation. Specimen 1 experienced little damage and was not near to penetration so it was not used. Specimens 7 and 8 had severe perforation and were not used to characterize the specimens. The impact energy, E_i, and absorbed energy, E_a, of these specimens are given in Table 5-1. The range of absorbed energy for penetration and perforation was 31.66 J to 34.17 J. The difference between E_i and E_a is also shown. These values indicate how much more absorbed energy would have been needed to put the data points on the equal energy line. The minimum value of them could be considered as the minimum energy not absorbed by the

specimens due to vibration and heat. The minimum difference was 0.86 J for the $L[(0/90)_6]$ specimens. The last column in Table 5-1 indicates whether the tup rebounded, Rb, penetrated, Pn, or perforated, Pr.

Table 5-1: $L[(0/90)_6]$ specimens.

Specimen	E_i (J)	E_a (J)	E_i-E_a (J)	Rb, Pn, Pr
1	33.15	29.57	3.58	Rb
*2	34.60	31.66	2.94	Rb
*3	35.29	33.11	2.19	Rb
*4	34.22	33.24	0.97	Rb
*5	35.03	34.17	0.86	Rb
*6	35.06	33.90	1.16	Pr
7	37.10	35.45	1.65	Pr
8	40.77	36.85	3.92	Pr
*Average	34.84	33.21		

Rb is rebounding, Pn is penetration, and Pr is perforation

5.1.2 Stitched Specimens

The stitched specimens produced the load-deflection curves shown in Figure 5-3. These curves seemed to be very consistent as they overlapped very well in the loading and unloading sections. They were used to establish the energy profile shown in Figure 5-4. Table 5-2 gives the impact energy and absorbed energy for specimens 5-7 as well as their difference and whether the tup rebounded, penetrated, or perforated. Only specimens 5-7 were used to characterize the penetration and perforation thresholds of the stitched specimens, while specimens 1-4 and 8 were not. Specimens 1-3 had the tup rebound while specimens 4 and 8 were largely perforated. They were not close to either the penetration threshold or the perforation threshold.

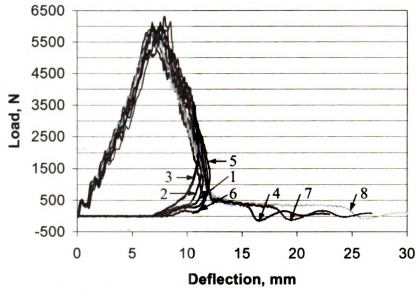

Figure 5-3: Load-deflection curves of S[(0/90)$_6$] specimens.

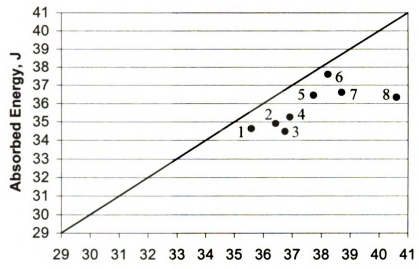

Figure 5-4: Energy profile of S[(0/90)$_6$] specimens.

The range for the penetration and perforation thresholds was from 36.61 J to 37.60 J. The unabsorbed energy was about 0.64 J as indicated in the fourth column of Table 5-2. The complete results are given in Appendix E.

Table 5-2: Stitched specimens.

Specimen	E_i (J)	E_a (J)	E_i-E_a (J)	Rb, Pn, Pr
1	35.58	34.63	0.96	Rb
2	36.42	34.90	1.52	Rb
3	36.75	34.48	2.27	Rb
4	36.91	35.25	1.66	Pr
*5	37.73	36.44	1.29	Rb
*6	38.24	37.60	0.64	Rb
*7	38.70	36.61	2.09	Pr
8	40.60	36.34	4.26	Pr
*Average	38.22	36.88		

Rb is rebounding, Pn is penetration, and Pr is perforation

5.1.3 Two-Dimensional Woven Specimens

The load-deflection curves of the 2D[$(\underline{0/90})_6$] specimens are shown in Figure 5-5. All of the curves are similar with overlapping along the loading and unloading sections. The corresponding energy profile is shown in Figure 5-6. The impact energy and absorbed energy values are given in Table 5-3. Specimens 1-4 were chosen to characterize the penetration and perforation resistance of these specimens. Specimens 1 and 3 had the tup rebound while specimens 2 and 4 were perforated. The remaining specimens were caused by large amounts of perforation so they were not used. The range of the penetration and perforation thresholds was 32.40 J to 35.86 J. The unabsorbed energy for specimen 3 was 0.07 J indicating that it was very close to the equal energy line. Column 5 of Table 5-3 indicated that the tup penetrated specimen 3 but did not perforate. This behavior gave a good indication of how much energy the specimens could absorb and no correction had to be made to the absorbed energy. The complete results are given in Appendix F.

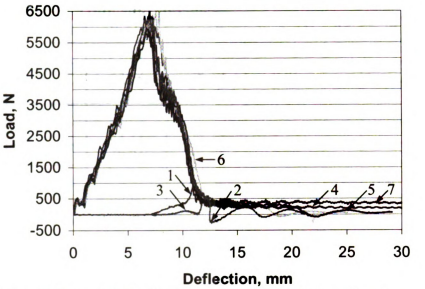

Figure 5-5: Load-deflection curves of 2D[(0/90)$_6$] specimens.

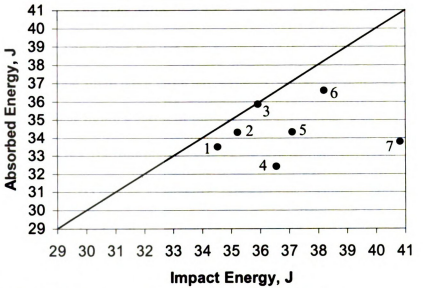

Figure 5-6: Energy profile of 2D[(0/90)$_6$] specimens.

Table 5-3: 2D[(0/90)$_6$] specimens.

Specimen	E_i (J)	E_a (J)	E_i-E_a (J)	Rb, Pn, Pr
*1	34.53	33.50	1.03	Rb
*2	35.22	34.30	0.92	Pr
*3	35.93	35.86	0.07	Pn
4	36.56	32.40	4.16	Pr
5	37.11	34.33	2.78	Pr
6	38.21	36.61	1.60	Pr
7	40.82	33.77	7.04	Pr
*Average	35.23	34.55		

Rb is rebounding, Pn is penetration, and Pr is perforation

5.1.4 Three-Dimensional Woven Specimens

Four three-dimensional woven plates, 3D[(0/θ)$_6$], were tested. The angles, θ, were 15°, 30°, 45°, and 90°. The load-deflection curves of the 3D[(0/90)$_6$] specimens are shown in Figure 5-7. The curves are not as consistent as the specimens mentioned earlier. This implies that there were large variations in the material properties of some of the specimens. This was likely a result of the fabricating process. The first 3D specimens made were the 3D[(0/90)$_6$] and it is likely that the weaving process was not refined. The remaining 3D woven specimens, presented in Appendix G, seemed to have smaller variations in the load-deflection curves which could be attributed to improved fabrication skills. The energy profile of the 3D[(0/90)$_6$] specimens is shown in Figure 5-8.

None of the data points are located right on the equal energy line. Specimens 3, 5, and 6 were used to characterize the penetration and perforation thresholds of the specimens. The penetration and perforation thresholds seemed to occur between 34.28 J and 35.75 J. The amount of unabsorbed energy was approximately 0.47 J. Specimen 4 was not used because its load-deflection curve was not similar to the others indicating that its material properties were different. Specimens 3 and 5 had the tup rebound, while specimen 6

experienced perforation. Specimen 1 had the tup rebound and was not close to penetration. Specimen 2 was perforated but its load-deflection curve was not matching the others so it was not used. Specimens 7 and 8 had large amounts of perforation and were not used. The impact energies and absorbed energies of the specimens are given in Table 5-4.

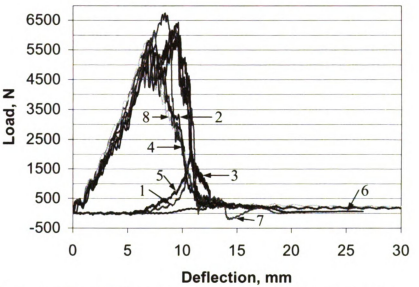

Figure 5-7: Load-deflection curves of 3D[(0/90)$_6$] specimens.

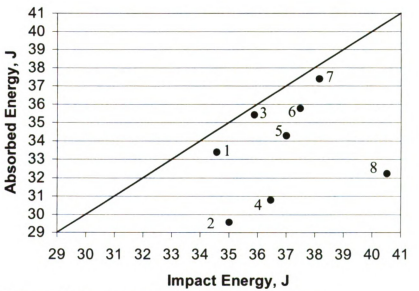

Figure 5-8: Energy profile of 3D[(0/90)$_6$] specimens.

Table 5-4: 3D[(0/90)$_6$] specimens.

Specimen	E_i (J)	E_a (J)	E_i-E_a (J)	Rb, Pn, Pr
1	34.57	33.38	1.19	Rb
2	35.02	29.56	5.46	Pr
*3	35.88	35.41	0.47	Rb
4	36.47	30.78	5.69	Pr
*5	37.00	34.28	2.73	Rb
*6	37.48	35.75	1.73	Pr
7	38.15	37.38	0.77	Pr
8	40.52	32.23	8.29	Pr
*Average	36.79	35.15		

Rb is rebounding, Pn is penetration, and Pr is perforation

5.2 Discussions

All specimens produced similar results when compared to the L[(0/90)$_6$] specimens. None of the specimens had impact energies exactly equal to their respective absorbed energies. An amount of energy less than 1 J seemed to be lost in the tests due to vibration and heat for all tests. The energy profiles produced from the testing data were not able to determine the exact penetration and perforation. None of the samples had a large impact energy interval between penetration and perforation. This was likely due to the specimens being very thin. There was no remaining material for the tup to penetrate into once it made initial penetration. The testing results did reveal a range of impact energies for each specimen where the tup would almost penetrate or just perforate.The range of impact energies seemed to be a method for characterizing the ballistic performance of each specimen.

5.2.1 Angle Effect

The testing results revealed that fiber orientation had an influence on penetration and perforation thresholds. Figure 5-9 showed that penetration and perforation thresholds, for laminated specimens, increased as the fiber angle, θ, was decreased. This was believed to

be caused by the bending stiffness mismatch in the specimens. The bending stiffness mismatch was dependent on the difference of fiber orientation between adjacent laminae. It increased as the difference of fiber orientations was increased. This bending stiffness mismatch caused the composite specimens to delaminate when the interlaminar stress was higher than the allowable levels. Once delamination formed, the tup could perforate the delaminated specimens easier than specimens that were not delaminated [5, 17, 19]. The results of Figure 5-9 seemed to support this hypothesis. Small values of θ caused the specimens to delaminate less, hence increasing the penetration and perforation thresholds. The $L[(0/90)_6]$ specimens had the largest bending stiffness mismatch causing the largest delamination, thus the lowest penetration and perforation thresholds. On the contrary, the $L[(0/7.5)_6]$ and $L[(0/15)_6]$ specimens had smaller bending stiffness mismatch causing less delamination, thus larger penetration and perforation thresholds.

The results of the three-dimensional woven specimens given in Figure 5-10 showed a similar dependence on fiber orientation except for a small discrepancy in the $3D[(\underline{0/90})_6]$ specimens. As mentioned earlier, the load-deflection curves of the $3D[(\underline{0/90})_6]$ were not as consistent as other cases and that might be responsible for the discrepancy.

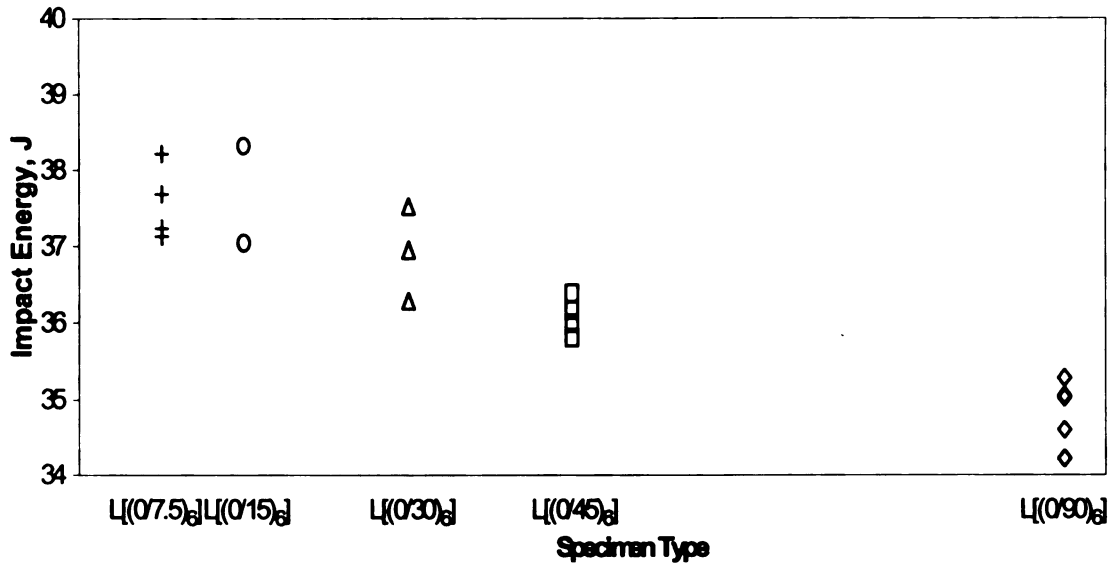

Figure 5-9: Impact energy interval of laminated specimens.

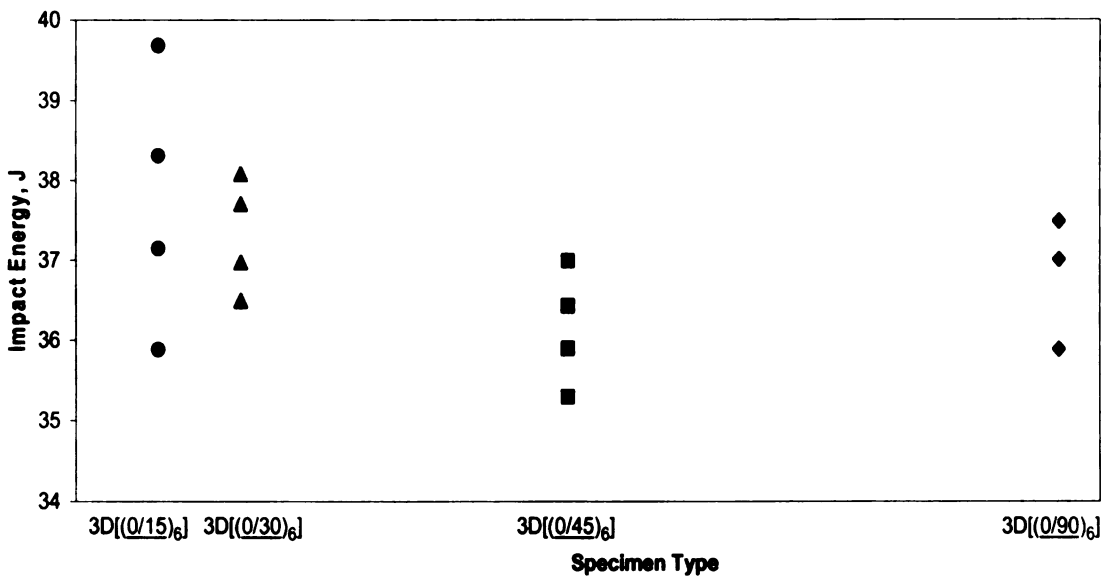

Figure 5-10: Impact energy interval of 3D specimens.

5.2.2 Through-Thickness Effect

The specimens tested have had varying degrees of through-thickness reinforcement. The laminated specimens had no through-thickness reinforcement. The only material joining the plies was the thin layer of matrix between them. There were no fibers contributing to any through-thickness strength.

The stitched specimens and laminated specimens were similar in that they were both initially $L[(0/90)_6]$ specimens. The stitched specimen used 1 mm wide strips of prepreg as stitching thread to join the plies together. Stitching through the thickness with a 12.5 mm x 12.5 mm square pattern proved to be the best through-thickness reinforcement method, among the composites tested, as shown in Figure 5-11. It was likely that this stitching pattern was an efficient selection. A stitching pattern with large dimensions may not have been efficient enough. On the other hand, a stitching pattern with smaller dimensions may have caused higher stress concentrations.

Each piece of the two-dimensional woven specimens consisted of two plies that were interwoven. This interweaving reinforced each piece. Six pieces were then stacked together to form the completed two-dimensional woven specimens. As a result, the two-dimensional woven specimens had more through-thickness reinforcement than the laminated specimens. This caused the two-dimensional woven specimens to require slightly more energy to begin penetration and perforation than the laminated specimens. Thus, the two-dimensional woven specimens had higher penetration and perforation thresholds than the laminated specimens.

The three-dimensional woven specimens were reinforced through the thickness by fibers although they were not oriented in the thickness direction. This made them more resistant to penetration and perforation when compared to the two-dimensional woven and laminated specimens.

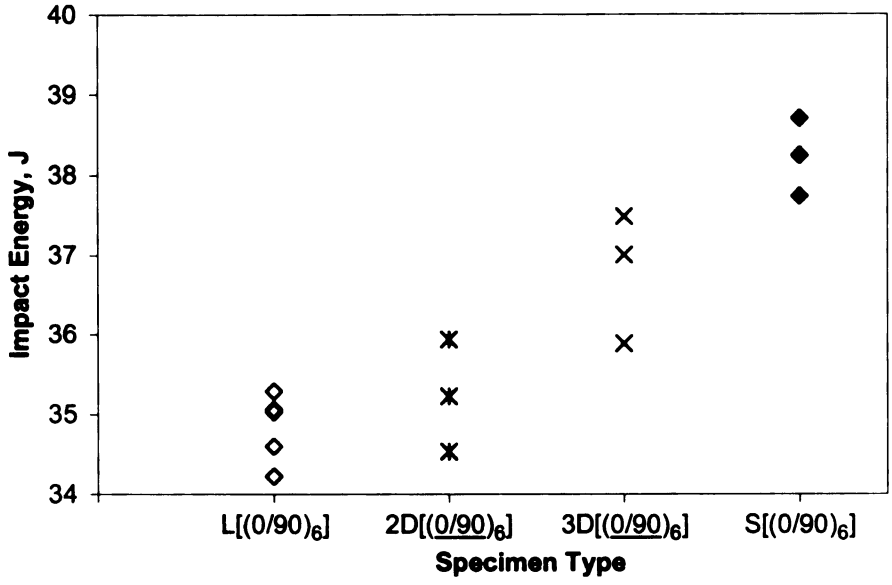

Figure 5-11: Impact energy interval of [(0/90)$_6$] specimens.

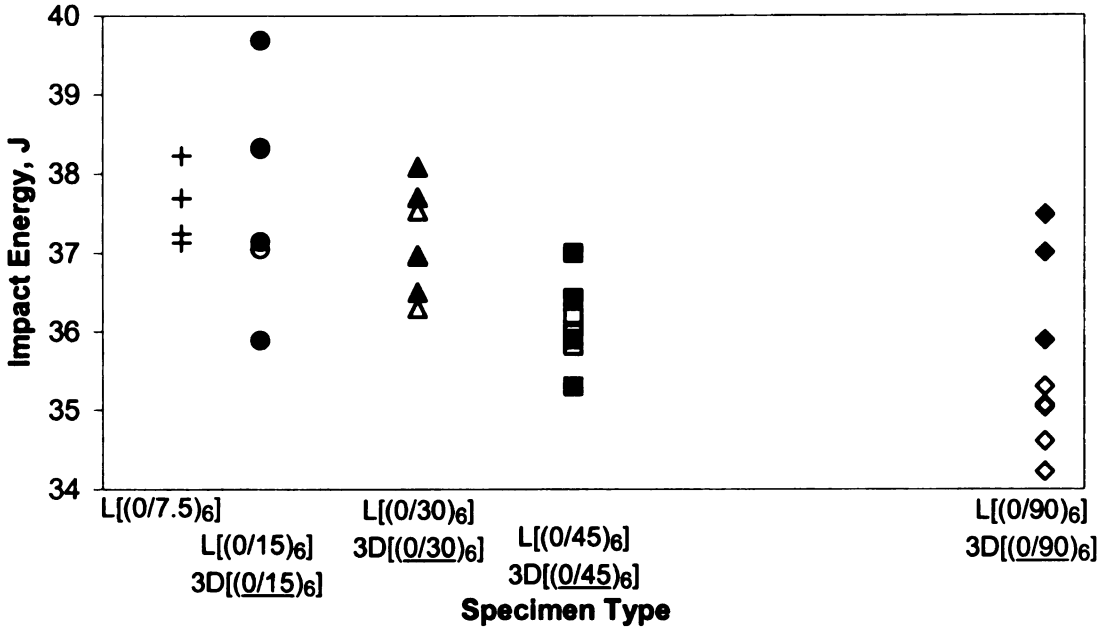

Figure 5-12: Impact energy interval of specimens with equal θ.

The 3D woven plates were fabricated with four different θ values that were 15°, 30°, 45°, and 90°. Four of the laminated plates shared the same θ values. The results from the testing of these specimens are shown in Figure 5-12. The solid symbols represent the 3D woven specimens. The L[(0/7.5)$_6$] results are shown for comparison. The 3D woven

specimens had larger energy intervals than the laminated specimens. This was the most obvious when looking at the results of the 3D[$(\underline{0/15})_6$] specimens. The 3D[$(\underline{0/30})_6$] specimens performed slightly better than L[$(0/30)_6$] specimens. The testing results showed less impact energy was required to begin perforation in the 3D[$(\underline{0/45})_6$] specimens when compared to the L[$(0/45)_6$] specimens. The energy interval for the 3D[$(\underline{0/45})_6$] specimens was larger while the energy to cause perforation was greater. The 3D[$(\underline{0/90})_6$] specimens showed the largest improvement on penetration and perforation resistance when compared to the L[$(0/90)_6$] specimens with the same θ value. The 3D woven specimens increased penetration resistance by nearly 1.7 J. Perforation resistance was increased by over 2 J. Visual inspection showed a decrease in delamination area, which seemed to not propagate as far from the impacted area as in the other specimens. The undulations in the 3D woven fabric seem to retard the delamination growth.

Figure 5-13 compares L[$(0/45)_6$] specimen 5 to 3D[$(\underline{0/45})_6$] specimen 6. They were subjected to impact energies of 36.39 J and 36.42 J, respectively. Delamination is shown by the darker areas of the specimens when the specimens are placed on a light table and photographed. The laminated specimen delaminated more than the 3D woven specimen. The delamination of the bottom ply extends almost the entire length of the specimen. The 3D woven specimen delamination seemed to be constrained to the center of the specimen; it passed slightly beyond the undulations of the warp and fill strips.

The delamination of 2D[$(\underline{0/90})_6$] specimen 1 and 3D[$(\underline{0/90})_6$] specimen 1 is compared in Figure 5-14. The specimens were impacted with energies of 34.53 J and 34.57 J, respectively. The delamination area of the 2D specimen was larger than the 3D specimen. The 2D specimen had delamination extend away from the

impact point. The 3D specimen seems to contain the delamination to an area close to the point of impact, i.e. at the center of the unit cell.

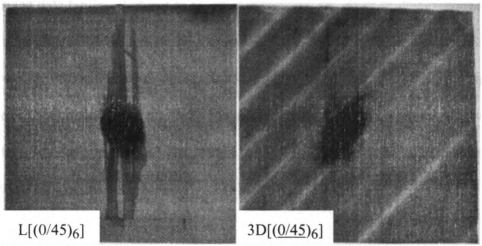

Figure 5-13: Delamination of L[(0/45)$_6$] and 3D[(0/45)$_6$] specimens.

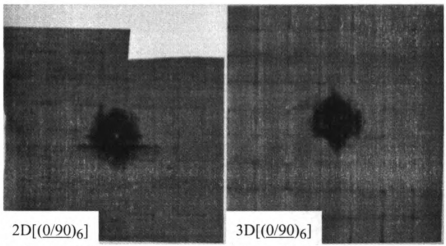

Figure 5-14: Delamination of 2D[(0/90)$_6$] and 3D[(0/90)$_6$] specimens.

5.3 Composite Damage

All specimens were damaged when they were impacted with the tup. The amount of damage depended on the impact energy and type of specimen. Figures 5-15 and 5-16 show the damage of the 3D[(0/45)$_6$] specimens observed from the top and bottom surfaces, respectively. The specimens were placed on a light table and photographed. The specimens are arranged in order of increasing impact energy. Each specimen is

labeled with its test number and impact energy. The numbers are consistent with those used in the corresponding load-deflection curves, energy profile diagrams, and summarized data tables. Pictures of all other specimens are given in Appendices H-K.

The dark area at the centers of the specimens is a combination of delamination and fiber breakage. Specimens 3-5 were penetrated so the tup did not pass through the specimens. Specimen 2 in Figure 5-15 has been perforated as light can be seen through the center. The dark regions are larger in Figure 5-16 as more delamination occurred on the bottoms of specimens.

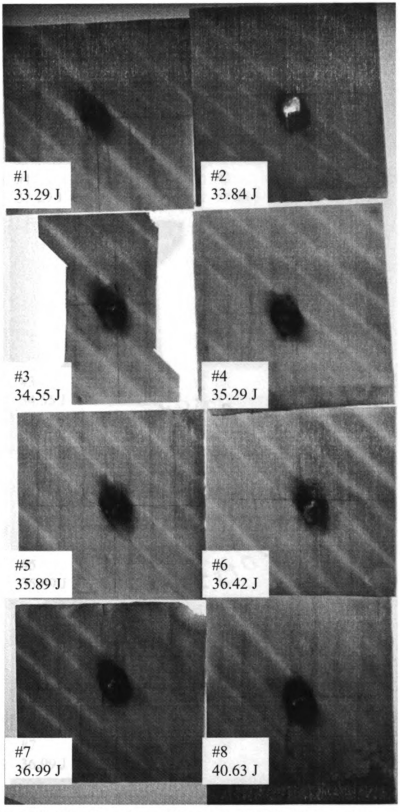

Figure 5-15: Top view of damage to 3D[$(0/45)_6$] specimens.

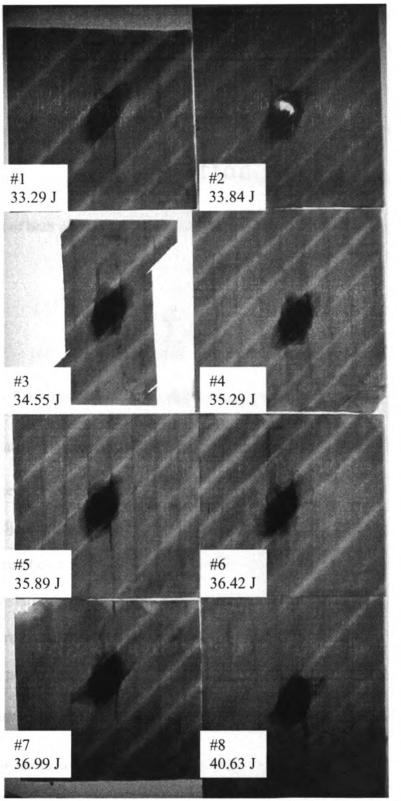

Figure 5-16: Bottom view of damage to 3D[$(\underline{0/45})_6$] specimens.

5.4 Material Behavior and Through-Thickness Reinforcement Hypotheses

The testing has shown that through-thickness reinforcement and small angles between adjacent plies increases penetration and perforation resistance. Plotting the normalized mismatch of D_{11} and D_{16} bending stiffness values for a two-ply laminate in Figure 5-17 reveals correlation with the testing results. The mismatch of D_{11}, has a value of zero when the fibers of both plies are in the same direction. D_{11} is calculated from Equation (5.1).

$$D_{11} = \frac{1}{3}\sum_{k=1}^{n} \bar{Q}_{11}(h_k^3 - h_{k-1}^3) \tag{5.1}$$

The mismatch of D_{11} has a maximum value when the angle between the adjacent plies is 90°. The mismatch of D_{11} can be correlated with the amount of delamination that occurs when composite plates are subjected to transverse load. There is no delamination when the fibers of adjacent layers are oriented in the same direction. The delamination area increases and reaches a maximum when the fibers in each ply are orthogonal to each other, i.e. the largest possible difference of fiber angles between adjacent plies. Delamination reduces a laminated composite to individual plies that can be easily penetrated and perforated.

The D_{16} mismatch curve seems to correlate with the penetration and perforation resistance of the laminated and 3D woven specimens. D_{16} is calculated from Equation (5.2).

$$D_{16} = \frac{1}{3}\sum_{k=1}^{n} \bar{Q}_{16}(h_k^3 - h_{k-1}^3) \tag{5.2}$$

The mismatch of D_{16} has a maximum value at 30°. The laminated and 3D woven specimens have their largest penetration and perforation thresholds at small θ values of 30° or less. It appears that both of these play a role in causing the specimens to absorb energy.

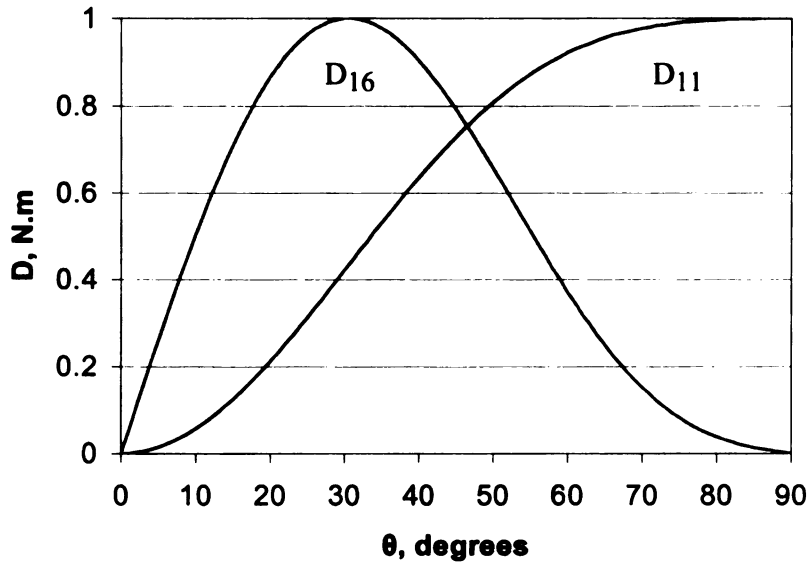

Figure 5-17: Normalized D_{11} and D_{16} values for two-ply laminate.

In addition, the through-thickness reinforcement seems to constrain the delamination cracks from spreading away from the impact points. Less delamination causes the tup greater difficulty in perforating the specimens.

A composite specimen with a D_{16} value not equal to zero indicates that when subjected to bending loads it will also twist, i.e. there is coupling. This coupling may change the direction of the tup on impact causing the tup to strike the specimen at an

angle of less than 90° to the specimen surface, i.e. oblique impact. Oblique impact could allow the specimens to have higher penetration and perforation resistance.

6. Conclusions and Future Study

6.1 Conclusions

Composite plates made from glass/epoxy were laminated, stitched, and woven with two-dimensional and three-dimensional fabric geometries. Laminated specimens constructed with θ angles of 7.5° and 15° had higher penetration and perforation resistance than specimens with θ angles of 30°, 45° and 90°. These results supported the hypothesis that small fiber angle values can increase penetration and perforation resistance. The stitched specimens had the largest penetration and perforation thresholds. The three-dimensional woven specimens outperformed the laminated and two-dimensional woven specimens. The 3D[$(\underline{0/15})_6$] and 3D[$(\underline{0/30})_6$] had larger penetration and perforation thresholds than the other three-dimensional specimens, which supports the fiber angle effect. The three-dimensional woven geometry was shown to have good impact resistance most likely due to the innovative way of linking each ply together.

6.2 Future Study

The time spent fabricating and testing specimens revealed many things that could be changed or made better to ensure testing gave the desired results.

The first area deals with creating the samples. The laminated samples were not difficult to create. Maintaining the correct fiber angle for each ply was important for creating good specimens. The fabrication of the stitched panel was time consuming because the thread would break often. Friction between the thread and needle eye and the thread and plies was the cause. The 2D woven and 3D woven samples would be more

easily made if a loom were used. A small handloom could be used for making the 2D woven fabric if dry fibers were used. Dry fibers would allow the tow width to be varied.

Testing had shown that the 3D woven geometry improved impact resistance when compared to laminated and 2D woven specimens. More testing could be conducted to reinforce the results of the current study. Other fibers could be tested such as carbon and Kevlar. Smaller tow widths would decrease the unit cell size possibly leading to an increase in the penetration and perforation thresholds. Automation of the weaving would increase the ability to test more fiber types and weaving angles while reducing the time needed to create each plate. The cost of a fully automated machine would be very expensive and a machine may not exist that could weave the 3D weave geometry. The best choice would be to modify a purchased loom so that the 3D weave geometry could be achieved. A loom would require dry roving to be used so the woven fabric would have to be infused with resin using a method such as vacuum assisted resin transfer molding or by pouring the resin directly onto the fabric before autoclaving.

Testing had been made more efficient with toggle clamps. These clamps ensured that all specimens were clamped at the same points and with the same pressures. The pneumatic rebound arrestor eliminated the need to catch the crosshead after it rebounded from the specimens. The load cell could be calibrated before more specimens were tested. Static calibration should be adequate, but dynamic calibration using a shock tube or other dynamic method would be better. Quasi-static loading does not accurately simulate the loading experienced during impact events.

The design of the tup should change for all future testing when penetration and perforation thresholds are being sought. The sides of the tup should not be able to rub on

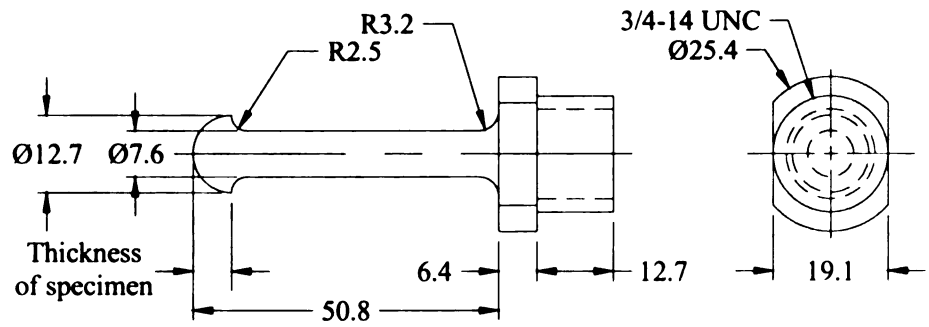

Figure 6-1: Proposed tup design.

the specimens and cause absorbed energy to be measured after the specimens are perforated. The proposed tup design shown in Figure 6-1 would greatly reduce the friction between the sides of the tup and the specimens. The tip of the tup should be the only portion that would contact the specimens. The tup would need to be hardened to prevent deformation and damage to its surface.

The autoclave could be instrumented with thermocouples to ensure that all plates were being cured with the same temperature. The curing of six panels at a time should be abandoned if the temperature is not uniform in the autoclave.

The software currently used with the instrumented drop weight tester is DOS based. All data recorded by the software had to be saved to a 3.5" disk then transferred to a computer running Microsoft Windows. Upgrading the software and computer so that data collection and subsequent analysis could be performed on the same machine would increase testing efficiency.

This study has revealed that more testing of the 3D woven fabric would be useful. Numerical analysis of the 3D weaving geometry could be used to understand better the behavior of the composite specimens during impact.

Appendices

Appendix A

Optical microscope images of cross sections of L[$(0/90)_6$], S[$(0/90)_6$], 2D[$\underline{(0/90)_6}$], and 3D[$\underline{(0/90)_6}$] specimens taken at a magnification of 120X

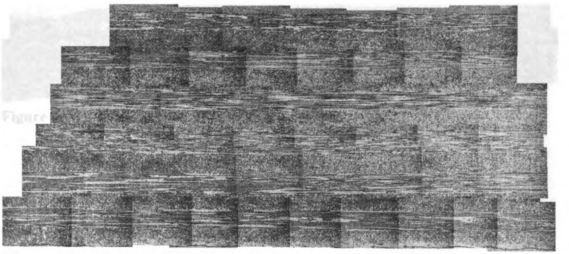

Figure A-1: Cross section of L[$(0/90)_6$] specimen.

Figure A-2: Cross section of S[$(0/90)_6$] specimen.

Figure A-3: Cross section of 2D[$\underline{(0/90)}_6$] specimen.

Figure A-4: Cross section of 3D[$\underline{(0/90)}_6$] specimen.

Appendix B

MATLAB program for calculating absorbed energy and impact energy

```
clear all

%%%%%%%%%%%%%%%%%%%%%%%%%%%%%%%%%%%%%%%%%%%%%%%%%%%%%%%%%%%%%%%%%%%%%%%
%   This program is written for English units (ft, lb, s)    %
%%%%%%%%%%%%%%%%%%%%%%%%%%%%%%%%%%%%%%%%%%%%%%%%%%%%%%%%%%%%%%%%%%%%%%%

%Import EXCEL data first '...' is file name. Second '...' is worksheet
name
data = xlsread('fullrawdatalubetest.xls', 'test6');

%Groups each column of data each with a different name
Point_Number = data(:,1);
Time = data(:,2)/1000;
Load = data(:,3);
Deflection = data(:,4)/12;
Velocity = data(:,5);
Energy = data(:,6);

%The Dynatup head weighs 11.0862 pounds.  This is correct.  Weighed in
Composites Center 2/04.
Mass = 11.0862/32.1740;

%Store point called zero_velocity which is velocity when tup impacts
plate
l=0;
for(i=1:length(Time));
    if(Time(i)==0);
        l=l+1;
        zero_velocity(l) = Velocity(i);
    end
end

New_acceleration = Load/Mass;

%Two methods for calculating the velocity difference using cumtrapz and
polyarea
Velocity_difference = cumtrapz(Time, New_acceleration);

Velocity_difference1 = max(Velocity_difference)

Velocity_difference2 = polyarea(Time, New_acceleration)

%Calculates the tup velocity at each increment
for(i=1:length(Velocity_difference));
    New_velocity(i) = (Velocity_difference(i)-zero_velocity)*-1;
end

%Calculates the displacement of the tup
New_displacement = cumtrapz(Time, New_velocity);

%Two methods for calculating the absorbed energy using cumtrapz and
polyarea
absorbed_energy = cumtrapz(New_displacement, Load);

New_absorbed_energy_ftlb = max(absorbed_energy)

Absorbed_energy1 = polyarea(New_displacement', Load)
```

```
%Calculate the impact energy with and without mgh'
New_kinetic_energy_ftlb = .5*Mass*zero_velocity.^2

New_kinetic_energy_w_mgh_ftlb = .5*Mass*zero_velocity.^2 +
Mass*32.174*max(New_displacement)

%Output the total deflection
Total_displacement_inches = max(New_displacement)*12

%Simpson's rule for calculating integral of New_acceleration*d(Time)
    n = (Time(length(Time),1) - Time(1,1))/(Time(2,1));
    width = Time(length(Time),1) - Time(1,1);
    for i=2:.5*n+1
        y(i)= New_acceleration(2*(i-1));
    end

    for j=2:.5*n
        z(j)= New_acceleration((2*j)-1);
    end

    Simpson_area_velocity = (width)*((New_acceleration(1,1) + 4*sum(y)
+ 2*sum(z) + New_acceleration(length(Time),1))/(3*n))

%Simpson's rule for calculating integral of New_velocity*d(Time)
    New_veloc = New_velocity';
    p = (Time(length(Time),1) - Time(1,1))/(Time(2,1));
    width = Time(length(Time),1) - Time(1,1);
    for i=2:.5*p+1
        y(i)= New_veloc(2*(i-1));
    end

    for j=2:.5*p
        z(j)= New_veloc((2*j)-1);
    end

    Simpson_area_displacement = ((width)*((New_veloc(1,1) + 4*sum(y) +
2*sum(z) + New_veloc(length(Time),1))/(3*p)))*12

%Plots
figure(1)
plot(Time, New_acceleration)
xlabel('Time (s)')
ylabel('Acceleration (ft/s^2)')
title('Acceleration vs. Time')

figure(2)
plot(Time, New_velocity)
xlabel('Time (s)')
ylabel('Velocity (ft/s)')
title('Velocity vs. Time')

figure(3)
plot(Time, New_displacement*12)
xlabel('Time (s)')
ylabel('Displacement (in)')
title('Displacement vs. Time')
```

```
figure(4)
plot(New_displacement*12, Load)
xlabel('Displacement (in)')
ylabel('Load (lbf)')
title('Load vs. Displacement')
```

Appendix C

Load cell calibration data

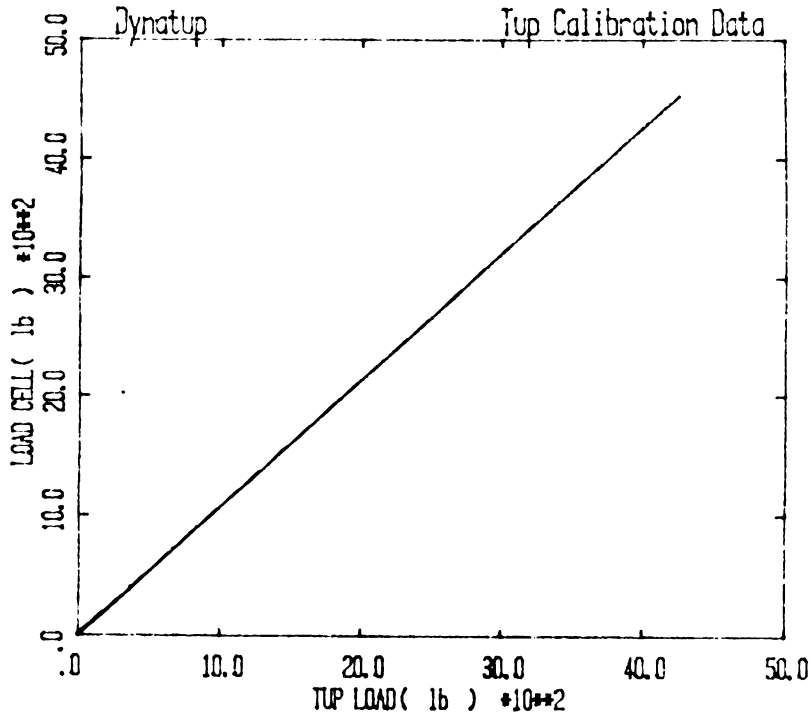

Tup Product No.: 8496-01 Maximum Tup Capacity: 5000 lbs 22241 N
Serial No.: 07645 Operator: Ray Smith
Approval: Customer: Michigan State University
Dynatup Job No.: 196771 Date: July 31, 2000

Bridge Resistances

A-E 861 Ohms	A-B 641 Ohms	A-D 645 Ohms
E-B 645 Ohms	E-D 645 Ohms	B-D 861 Ohms

Gage Pair Balance

(A-E, B-D) 0 Ohms	(A-B, E-D) 4 Ohms	(A-D, E-D) 0 Ohms

Collective Balance	50mV Test	
(A-B, E-B, A-D, E-D)	4 Ohms	10 mV
Temperature at Calibration	73.6 degrees F.	23.1 degrees C.

Calibration is traceable to NIST; NVLAP #105023-0

Tup Calibration Factor	Load Range
3326 lb 14749 N	1000 lb 4448 N
3327 lb 14799 N	2000 lb 8896 N
3326 lb 14749 N	3000 lb 13344 N
3322 lb 14776 N	4000 lb 17792 N
3320 lb 14768 N	5000 lb 22241 N

Figure C-1: Load-cell calibration data

Appendix D

Load-deflection curves and energy profiles of laminated specimens

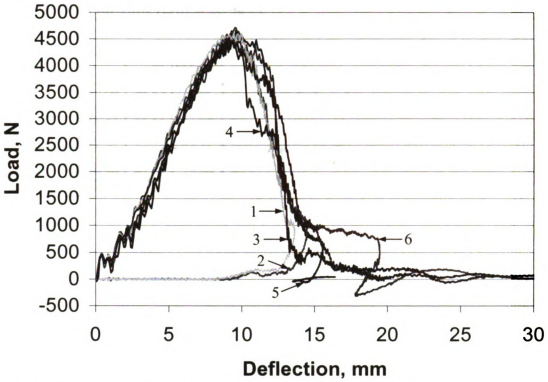

Figure D-1: Load-deflection curves of L[(0/7.5)$_6$] specimens.

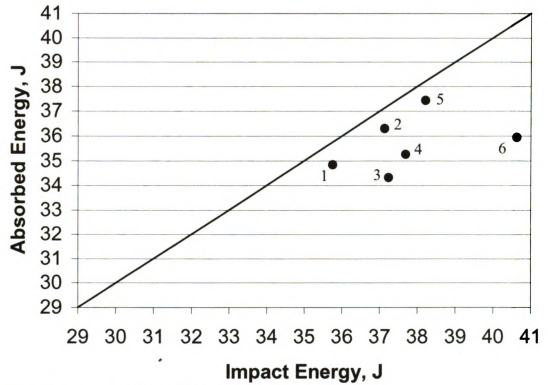

Figure D-2: Energy profile of L[(0/7.5)$_6$] specimens.

Table D-1: Data for L[(0/7.5)$_6$] specimens.

		Software Results			Velocity Based Correction Method				Extended Method		
Specimen	Tup	E_i (J)	E_a (J)	h' (mm)	E_i (J)	E_a (J)	E_i-E_a (J)	h' (mm)	E_i (J)	E_a (J)	h' (mm)
1	Rb	35.09	34.83	8.38	35.76	34.83	0.93	13.63	35.73	35.29	13.30
*2	Rb	36.42	36.30	9.40	37.13	36.30	0.84	14.48	37.08	36.04	13.70
*3	Pr	36.58	36.82	23.37	37.24	34.30	2.93	13.31	37.23	34.29	13.30
*4	Pr	36.99	37.16	23.37	37.69	35.25	2.44	14.22	37.98	36.74	16.30
*5	Pn	37.50	38.11	14.73	38.22	37.42	0.80	14.48	38.22	37.57	14.90
6	Pr	39.94	40.72	18.54	40.63	35.93	4.70	13.89	40.59	34.92	13.50
* Average		36.87	37.10		37.57	35.82			37.63	36.16	

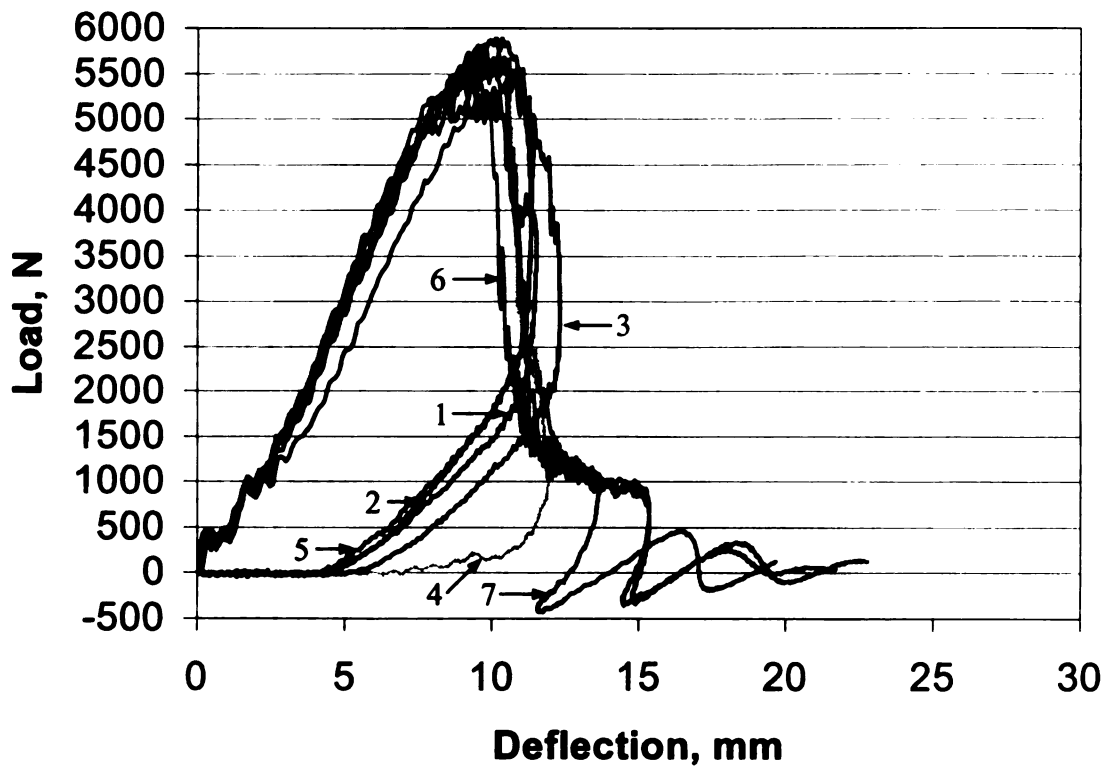

Figure D-3: Load-deflection curves of L[(0/15)$_6$] specimens.

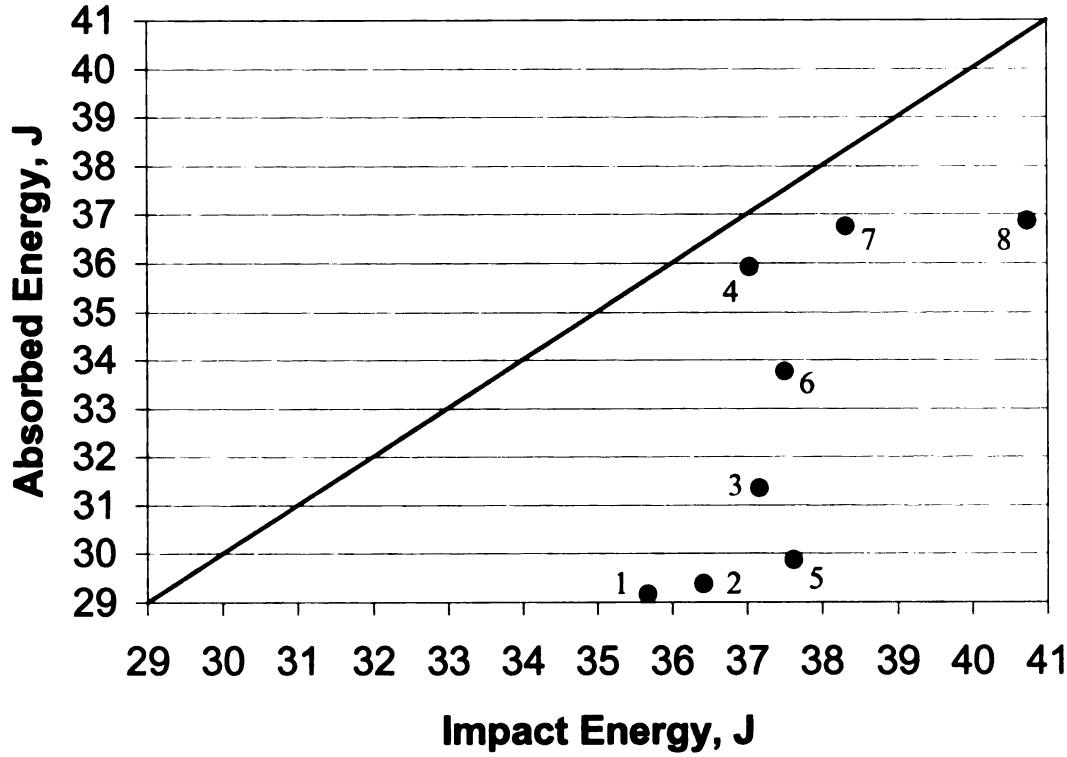

Figure D-4: Energy profile of L[(0/15)$_6$] specimens.

Table D-2: Data for L[(0/15)$_6$] specimens.

		Software Results			Velocity Based Correction Method				Extended Method		
Specimen	Tup	E_i (J)	E_a (J)	h' (mm)	E_i (J)	E_a (J)	E_i-E_a (J)	h' (mm)	E_i (J)	E_a (J)	h' (mm)
1	Rb	35.10	29.16	4.06	35.67	29.16	6.51	11.53	-	-	-
2	Rb	35.86	29.37	4.57	36.42	29.37	7.05	11.33	-	-	-
3	Rb	36.55	31.33	5.33	37.16	31.33	5.83	12.32	37.15	37.15	12.40
*4	Rb	36.44	35.92	7.11	37.04	35.92	1.12	12.01	36.99	35.39	11.30
5	Rb	37.05	29.87	4.32	37.62	29.87	7.75	11.40	-	-	-
6	Pr	36.93	37.79	18.54	37.50	33.76	3.74	11.43	37.59	32.15	10.70
*7	Pr	37.72	38.09	12.70	38.32	36.74	1.58	12.19	38.28	35.06	11.50
8	Pr	40.16	40.80	14.99	40.73	36.86	3.87	11.63	40.73	37.10	12.00
* Average		37.08	37.01		37.68	36.33			37.64	35.23	

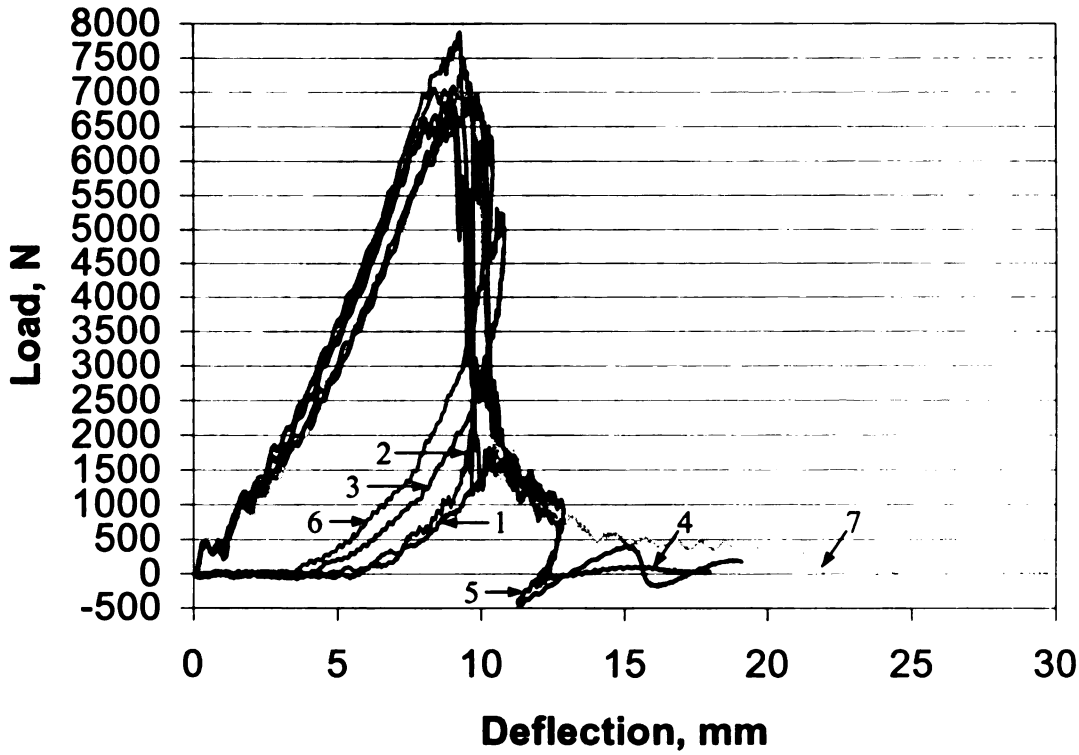

Figure D-5: Load-deflection curves of L[(0/30)$_6$] specimens.

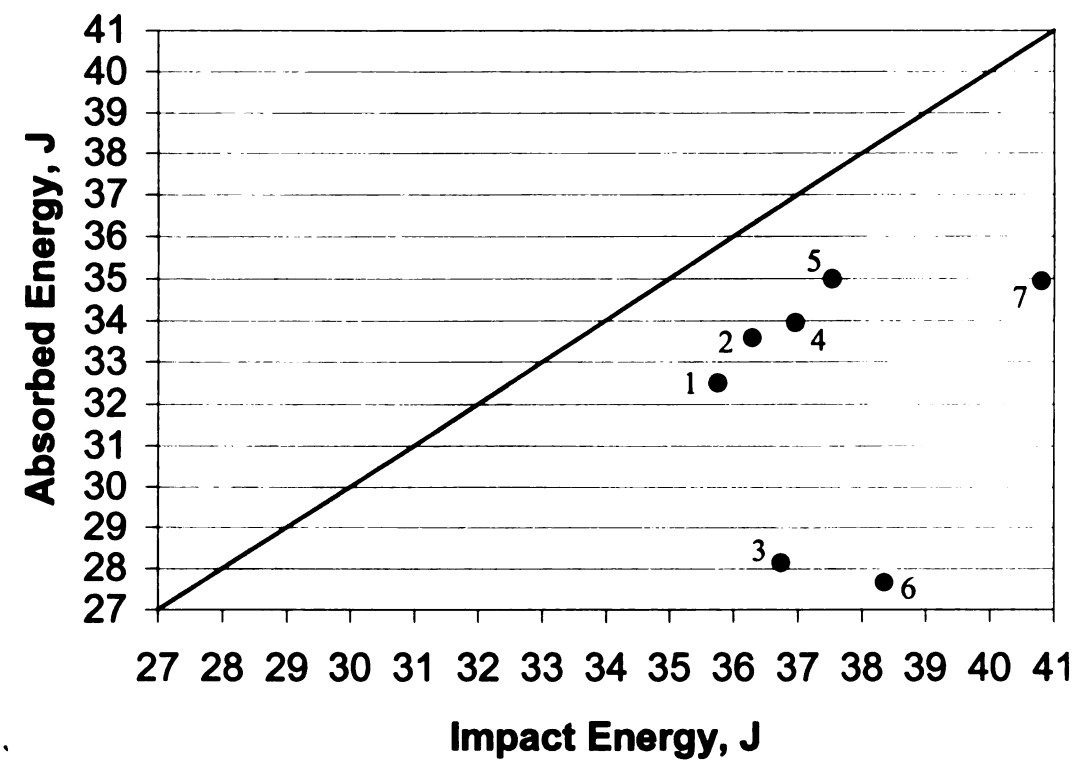

Figure D-6: Energy profile of L[(0/30)$_6$] specimens.

Table D-3: Data for L[(0/30)$_6$] specimens.

		Software Results			Velocity Based Correction Method				Extended Method		
Specimen	Tup	E_i (J)	E_a (J)	h' (mm)	E_i (J)	E_a (J)	E_i-E_a (J)	h' (mm)	E_i (J)	E_a (J)	h' (mm)
1	Rb	35.24	32.49	5.84	35.76	32.49	3.27	10.59	35.74	35.25	10.40
*2	Rb	35.81	33.57	5.08	36.29	33.57	2.72	9.73	36.28	36.48	9.80
3	Rb	36.21	28.13	4.06	36.75	28.13	8.61	10.82	-	-	-
*4	Pr	36.49	37.00	12.19	36.96	33.94	3.02	10.16	36.93	33.60	9.90
*5	Pr	37.00	37.39	12.19	37.53	34.98	2.55	10.82	37.48	32.40	9.80
6	Rb	37.84	27.67	3.56	38.35	27.67	10.68	10.42	-	-	-
7	Pr	40.15	41.18	22.10	40.81	34.93	5.88	13.46	40.66	34.37	10.70
* Average		36.43	35.99		36.93	34.16			36.90	34.16	

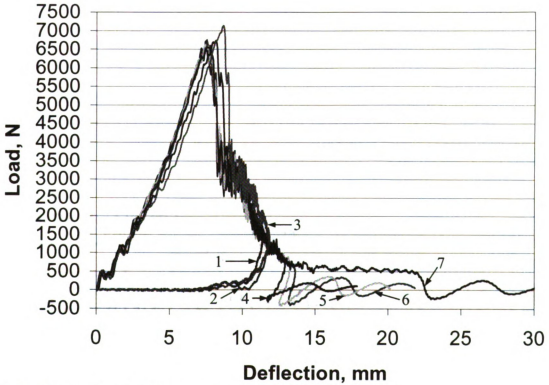

Figure D-7: Load-deflection curves of L[(0/45)$_6$] specimens.

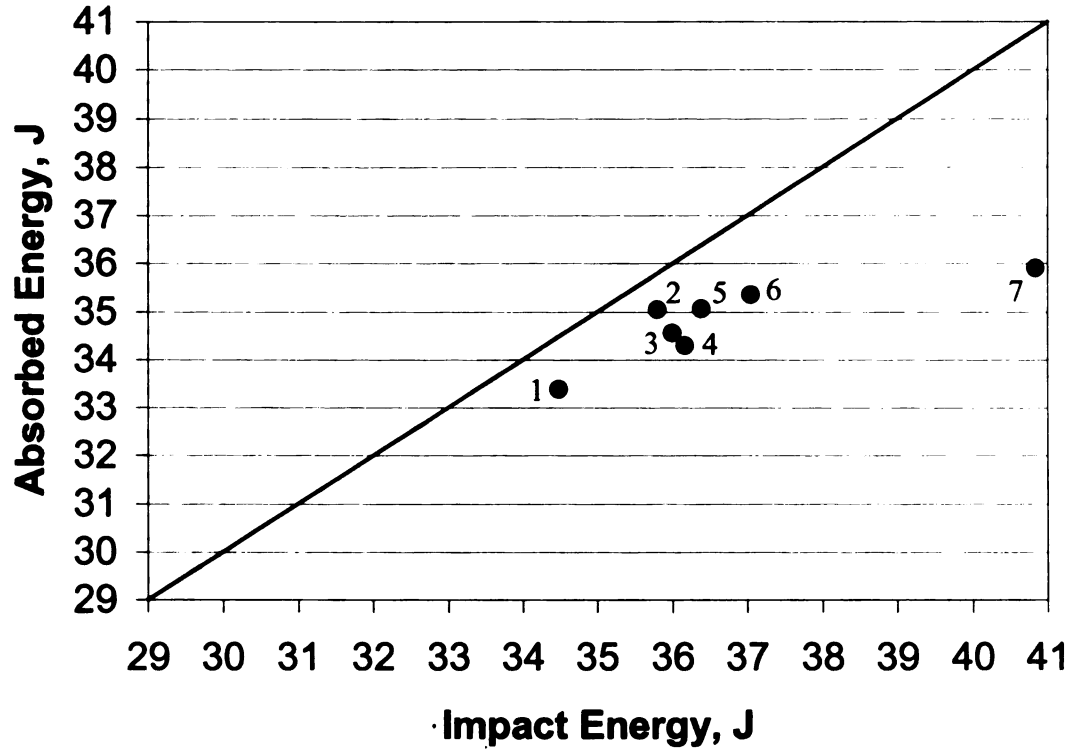

Figure D-8: Energy profile of L[(0/45)$_6$] specimens.

Table D-4: Data for L[(0/45)$_6$] specimens.

		Software Results			Velocity Based Correction Method				Extended Method		
Specimen	Tup	E_i (J)	E_a (J)	h' (mm)	E_i (J)	E_a (J)	E_i-E_a (J)	h' (mm)	E_i (J)	E_a (J)	h' (mm)
1	Rb	33.92	33.38	7.11	34.48	33.38	1.10	11.38	34.55	35.67	13.00
*2	Rb	35.22	35.03	7.87	35.81	35.03	0.77	11.79	35.88	36.83	13.50
*3	Rb	35.41	34.55	6.86	36.00	34.55	1.45	11.87	36.05	36.96	13.20
*4	Pr	35.62	36.12	12.70	36.17	34.29	1.88	11.18	36.25	35.93	12.60
*5	Pr	35.81	36.38	12.95	36.39	35.06	1.33	11.81	36.43	35.86	12.70
6	Pr	36.47	37.11	13.46	37.05	35.35	1.70	11.68	37.10	36.18	12.80
7	Pr	40.21	41.31	22.61	40.85	35.90	4.94	12.85	40.84	35.75	12.80
* Average		35.52	35.52		36.09	34.73			36.15	36.40	

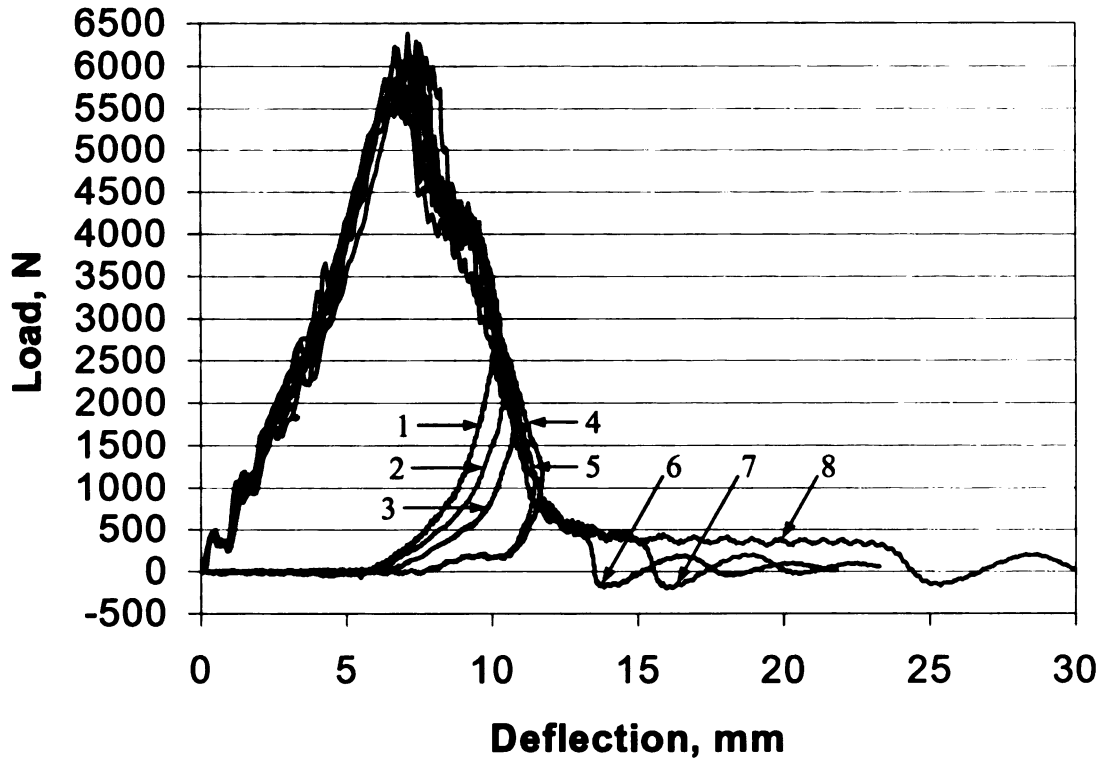

Figure D-9: Load-deflection curves of L[(0/90)$_6$] specimens.

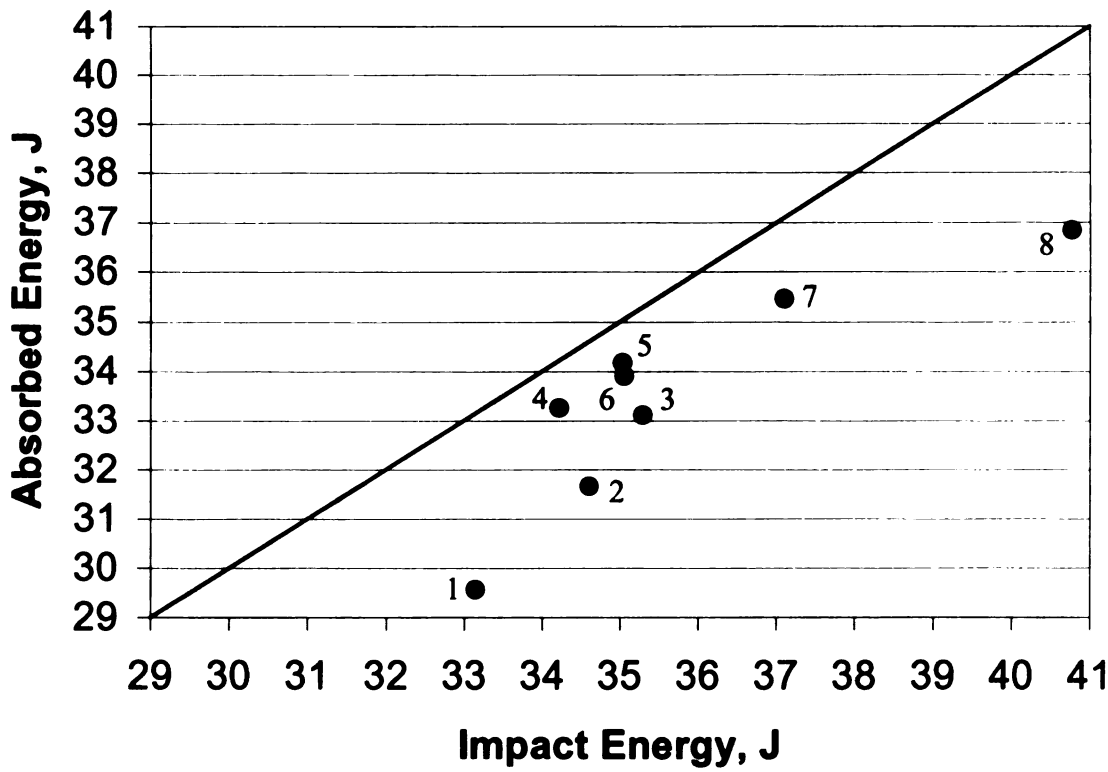

Figure D-10: Energy profile of L[(0/90)$_6$] specimens.

Table D-5: Data for L[$(0/90)_6$] specimens.

		Software Results			Velocity Based Correction Method				Extended Method		
Specimen	Tup	E_i (J)	E_a (J)	h' (mm)	E_i (J)	E_a (J)	E_i-E_a (J)	h' (mm)	E_i (J)	E_a (J)	h' (mm)
1	Rb	32.65	29.57	10.15	33.15	29.57	3.58	10.15	-	-	-
*2	Rb	34.09	31.66	10.46	34.60	31.66	2.94	10.46	-	-	-
*3	Rb	34.76	33.11	10.77	35.29	33.11	2.18	10.77	35.32	36.00	11.50
*4	Rb	33.64	33.24	11.72	34.22	33.24	0.98	11.72	34.26	34.89	12.80
*5	Rb	34.46	34.17	11.47	35.03	34.17	0.86	11.47	35.04	35.23	11.80
*6	Pr	34.49	35.16	13.46	35.06	33.90	1.16	11.43	35.07	34.14	11.80
7	Pr	36.53	37.27	15.49	37.10	35.45	1.65	11.68	37.11	35.70	12.20
8	Pr	40.16	41.28	24.38	40.77	36.85	3.92	12.45	40.73	36.10	11.80
* Average		34.29	33.47		34.84	33.22			34.92	35.07	

Appendix E

Load-deflection curves and energy profile of stitched specimens

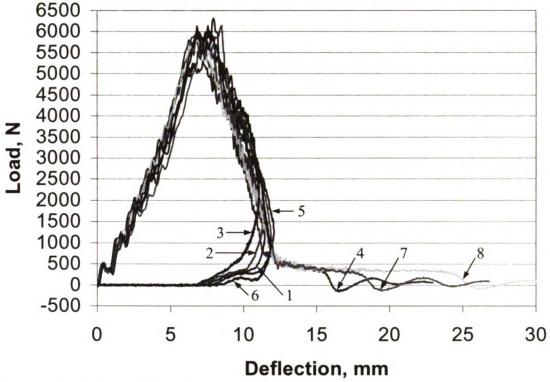

Figure E-1: Load-deflection curves of S[(0/90)$_6$] specimens.

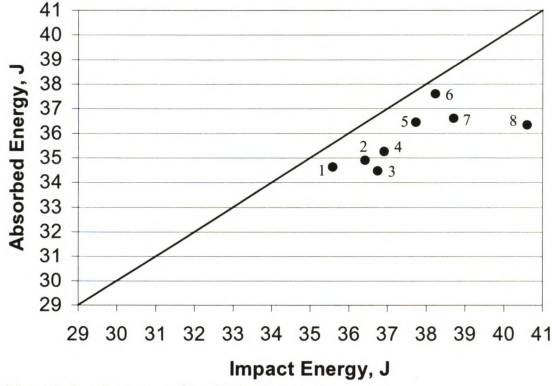

Figure E-2: Energy profile of S[(0/90)$_6$] specimens.

Table E-1: Data for S[(0/90)$_6$] specimens.

		Software Results			Velocity Based Correction Method				Extended Method		
Specimen	Tup	E_i (J)	E_a (J)	h' (mm)	E_i (J)	E_a (J)	E_i-E_a (J)	h' (mm)	E_i (J)	E_a (J)	h' (mm)
1	Rb	35.02	34.63	11.94	35.58	34.63	0.96	11.43	35.82	36.32	12.40
2	Rb	35.86	34.90	7.62	36.42	34.90	1.52	11.35	36.49	37.29	12.40
3	Rb	36.20	34.48	6.86	36.75	34.48	2.27	11.07	36.82	38.75	12.70
4	Pr	36.35	37.31	19.81	36.91	35.25	1.66	11.43	37.09	35.27	11.70
*5	Rb	37.14	36.44	7.87	37.73	36.44	1.29	12.10	37.77	38.46	13.10
*6	Rb	37.65	37.60	8.13	38.24	37.60	0.64	11.86	38.25	38.45	12.30
*7	Pr	38.10	38.97	18.80	38.70	36.61	2.09	12.19	38.69	36.64	12.40
8	Pr	40.01	41.15	25.40	40.60	36.34	4.26	11.94	40.62	36.45	12.50
* Average		37.63	37.67		38.22	36.88			38.24	37.85	

Appendix F

Load-deflection curves and energy profile of two-dimensional woven specimens

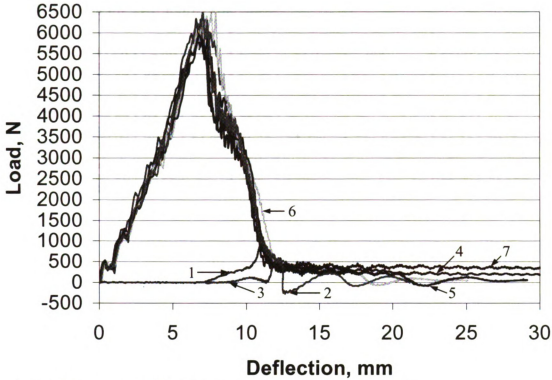

Figure F-1: Load-deflection curves of 2D[(0/90)$_6$] specimens.

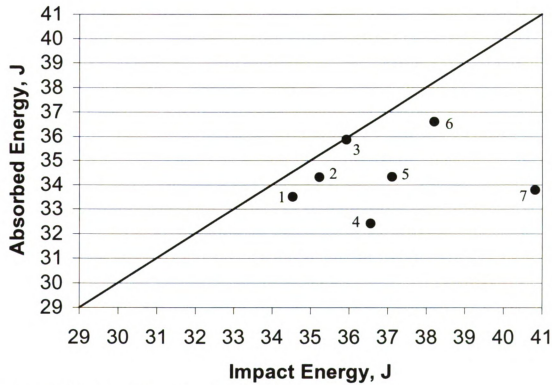

Figure F-2: Energy profile of 2D[(0/90)$_6$] specimens.

Table F-1: Data for 2D[$(0/90)_6$] specimens.

		Software Results			Velocity Based Correction Method				Extended Method		
Specimen	Tup	E_i (J)	E_a (J)	h' (mm)	E_i (J)	E_a (J)	E_i-E_a (J)	h' (mm)	E_i (J)	E_a (J)	h' (mm)
*1	Rb	33.99	33.50	7.87	34.53	33.50	1.03	11.02	34.58	34.90	11.60
*2	Pr	34.68	35.29	12.45	35.22	34.30	0.92	10.92	35.22	34.30	11.10
*3	Pn	35.35	35.86	11.43	35.93	35.86	0.07	11.79	35.95	36.12	12.50
4	Pr	36.00	37.49	34.80	36.56	32.40	4.16	11.43	36.52	31.96	10.90
5	Pr	36.55	37.47	21.34	37.11	34.33	2.78	11.35	37.11	34.36	11.50
6	Pr	37.62	38.52	19.30	38.21	36.61	1.60	11.89	38.25	36.52	11.90
7	Pr	40.27	41.81	33.27	40.82	33.77	7.04	11.18	40.80	33.67	11.10
* Average		34.67	34.88		35.23	34.56			35.25	35.11	

Appendix G

Load-deflection curves and energy profiles of three-dimensional woven specimens

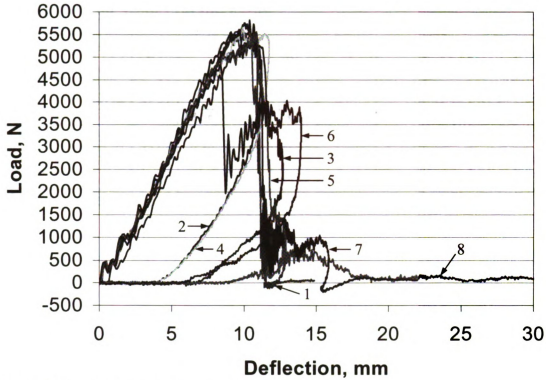

Figure G-1: Load-deflection curves of 3D[(0/15)$_6$] specimens.

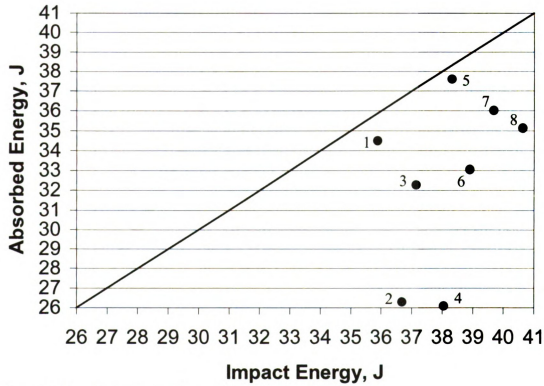

Figure G-2: Energy profile of 3D[(0/15)$_6$] specimens.

Table G-1: Data for 3D[(0/15)$_6$] specimens.

		Software Results			Velocity Based Correction Method				Extended Method		
Specimen	Tup	E_i (J)	E_a (J)	h' (mm)	E_i (J)	E_a (J)	E_i-E_a (J)	h' (mm)	E_i (J)	E_a (J)	h' (mm)
*1	Pr	35.33	34.78	11.43	35.88	34.49	1.39	11.18	35.88	34.51	11.20
2	Rb	36.13	26.29	3.81	36.69	26.29	10.40	11.22	-	-	-
3	Rb	36.54	32.27	6.86	37.14	32.27	4.87	12.13	37.16	37.26	12.20
4	Rb	37.47	26.09	3.56	38.05	26.09	11.97	11.75	-	-	-
*5	Pr	37.68	37.58	8.89	38.31	37.58	0.73	12.90	38.26	36.97	12.00
6	Pr	38.21	33.04	9.40	38.90	33.04	5.85	13.97	-	-	-
7	Pr	39.12	39.85	15.49	39.68	36.00	3.68	11.43	39.67	36.02	11.50
8	Pr	40.05	40.95	55.12	40.64	35.12	5.52	11.94	40.59	34.01	11.20
* Average		36.51	36.18		37.10	36.04			37.07	35.74	

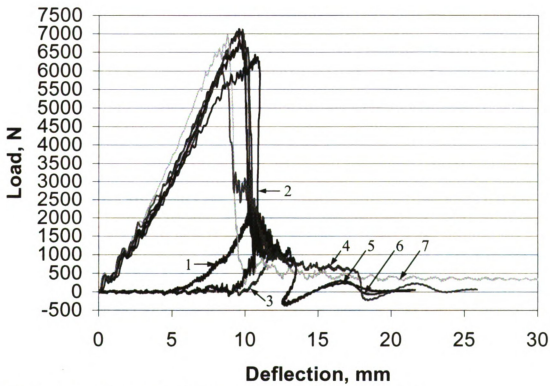

Figure G-3: Load-deflection curves of 3D[(0/30)$_6$] specimens.

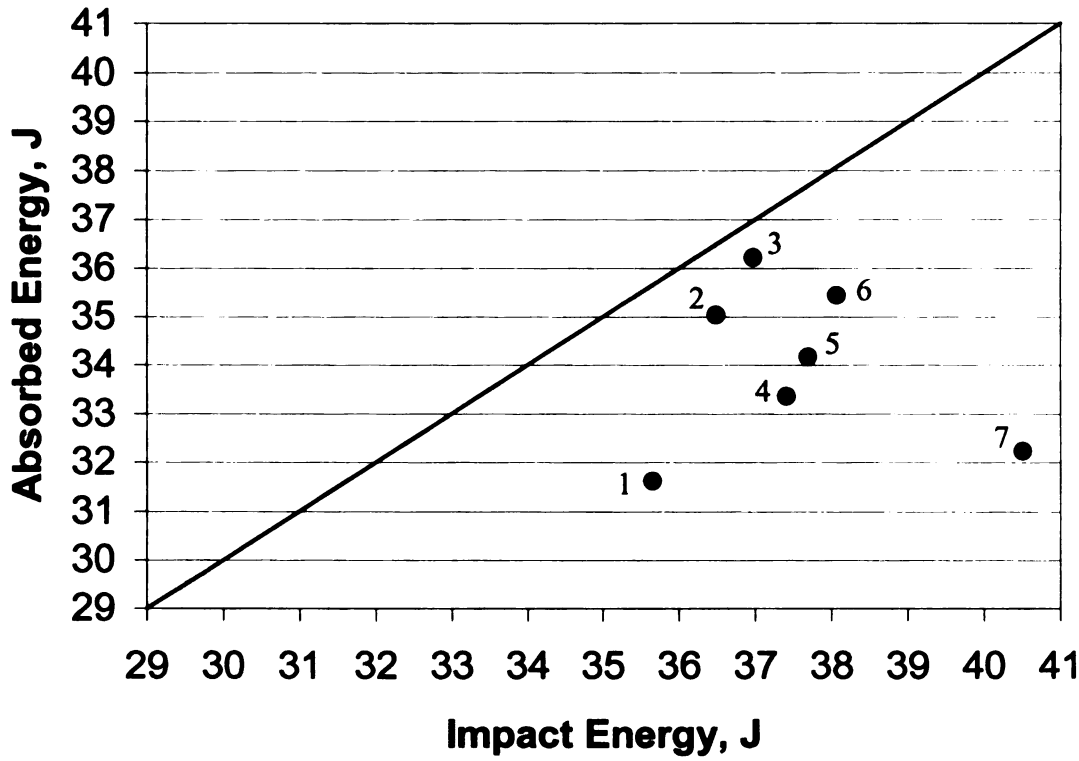

Figure G-4: Energy profile of 3D[(0/30)$_6$] specimens.

Table G-2: Data for 3D[(0/30)$_6$] specimens.

		Software Results			Velocity Based Correction Method				Extended Method		
Specimen	Tup	E_i (J)	E_a (J)	h' (mm)	E_i (J)	E_a (J)	E_i-E_a (J)	h' (mm)	E_i (J)	E_a (J)	h' (mm)
1	Rb	35.14	31.62	4.83	35.66	31.62	4.04	10.41	35.63	35.01	10.20
*2	Pn	35.94	35.02	9.14	36.49	35.02	1.46	10.99	36.47	36.52	11.00
*3	Pn	36.39	36.21	10.16	36.97	36.21	0.76	11.78	36.89	34.73	10.40
4	Pr	36.84	37.72	18.03	37.41	33.35	4.06	11.68	37.29	28.04	9.40
5	Pr	37.18	37.73	12.95	37.70	34.17	3.53	10.57	37.67	33.58	10.30
*6	Pr	37.54	38.11	12.95	38.08	35.43	2.65	10.80	38.05	34.92	10.50
7	Pr	40.01	41.56	33.78	40.51	32.23	8.28	10.03	40.47	31.88	9.60
* Average		36.62	36.45		37.18	35.55			37.14	35.39	

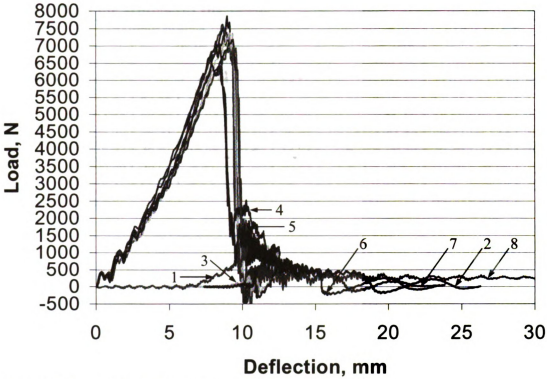

Figure G-5: Load-deflection curves of 3D[(0/45)$_6$] specimens.

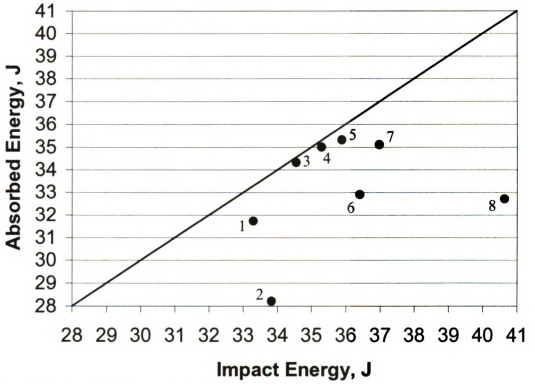

Figure G-6: Energy profile of 3D[(0/45)$_6$] specimens.

Table G-3: Data for 3D[(0/45)$_6$] specimens.

		Software Results			Velocity Based Correction Method				Extended Method		
Specimen	Tup	E_i (J)	E_a (J)	h' (mm)	E_i (J)	E_a (J)	E_i-E_a (J)	h' (mm)	E_i (J)	E_a (J)	h' (mm)
1	Rb	32.78	31.73	6.86	33.29	31.73	1.57	10.35	33.27	32.71	10.00
2	Pr	33.37	34.28	18.80	33.84	28.20	5.64	9.55	33.83	28.23	9.60
3	Pn	33.94	34.32	11.68	34.55	34.32	0.24	12.49	34.41	31.64	10.00
*4	Pn	34.67	35.00	11.68	35.29	34.99	0.29	12.56	35.12	30.08	9.50
*5	Pn	35.32	35.31	11.07	35.89	35.31	0.58	11.53	35.78	32.77	9.70
6	Pr	35.92	36.67	15.49	36.42	32.91	3.51	10.16	36.40	32.83	10.10
*7	Pr	36.50	35.09	9.91	36.99	35.09	1.90	9.91	36.98	34.98	9.80
8	Pr	40.15	32.72	9.91	40.63	32.72	7.92	9.91	40.61	32.58	9.70
* Average		35.50	35.13		36.05	35.13			35.96	32.61	

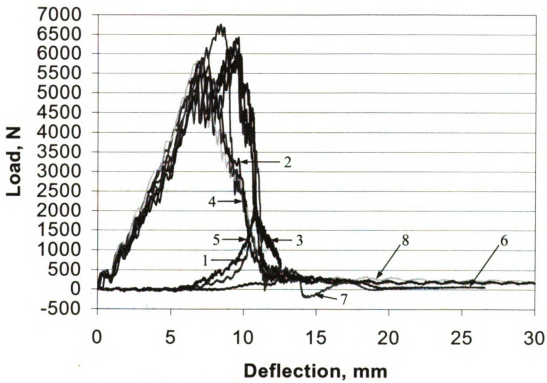

Figure G-7: Load-deflection curves of 3D[(0/90)$_6$] specimens.

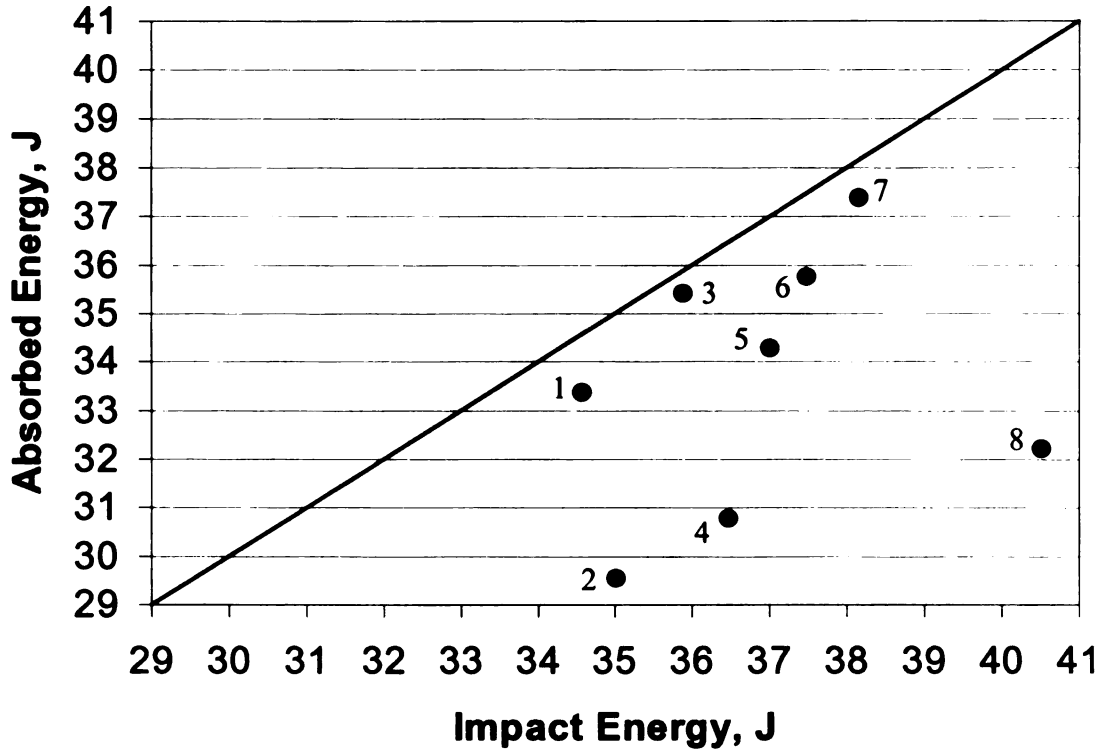

Figure G-8: Energy profile of 3D[(0/90)$_6$] specimens.

Table G-4: Data for 3D[(0/90)$_6$] specimens.

		Software Results			Velocity Based Correction Method				Extended Method		
Specimen	Tup	E_i (J)	E_a (J)	h' (mm)	E_i (J)	E_a (J)	E_i-E_a (J)	h' (mm)	E_i (J)	E_a (J)	h' (mm)
1	Rb	34.06	33.38	6.60	34.57	33.38	1.19	10.40	34.56	34.63	10.50
2	Pr	34.45	36.30	54.36	35.02	29.56	5.46	11.43	35.14	29.18	11.00
*3	Rb	35.28	35.41	8.64	35.88	35.41	0.47	12.29	35.94	36.19	13.50
4	Pr	35.92	37.87	53.34	36.47	30.78	5.69	11.18	36.46	30.82	11.30
*5	Rb	36.47	34.28	5.59	37.00	34.28	2.73	10.77	36.99	37.05	10.80
*6	Pr	36.92	37.90	23.11	37.48	35.75	1.73	11.43	37.62	35.45	11.10
7	Pr	37.56	37.38	14.73	38.15	37.38	0.77	12.07	38.27	37.38	11.50
8	Pr	39.96	40.40	47.24	40.52	32.23	8.29	11.43	40.51	32.22	11.50
* Average		36.22	35.86		36.79	35.15			36.85	36.23	

Appendix H

Laminated specimen damage

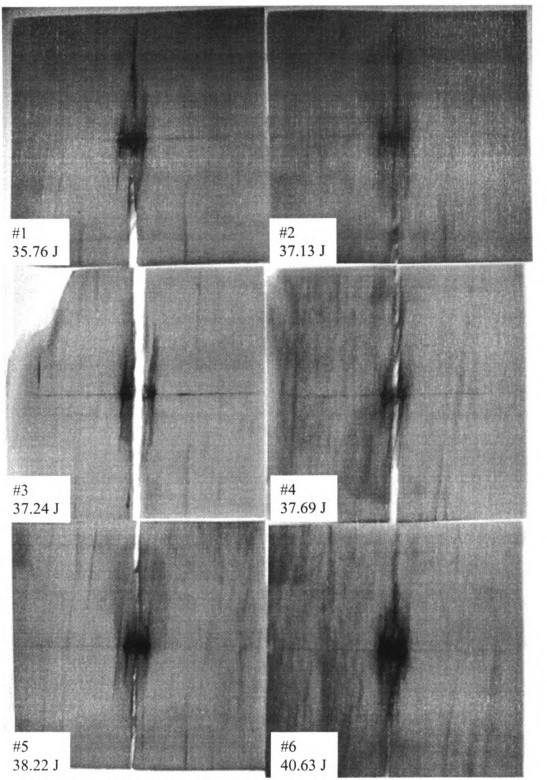

Figure H-1: Top view of damage to L[(0/7.5)$_6$] specimens.

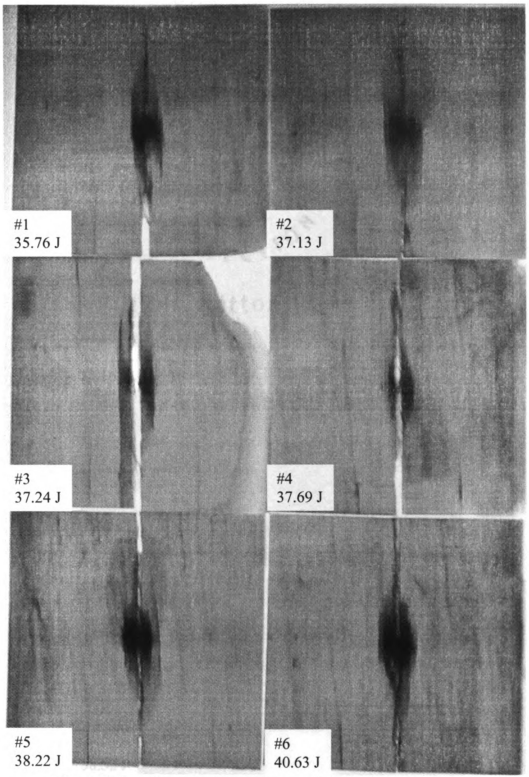

Figure H-2: Bottom view of damage to L[(0/7.5)$_6$] specimens.

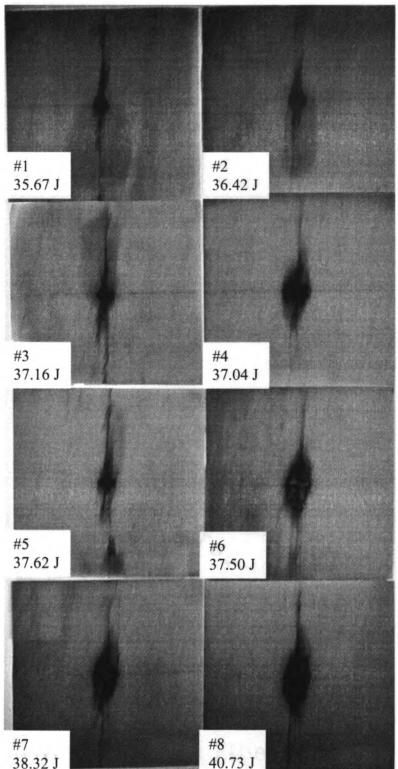

Figure H-3: Top view of damage to L[(0/15)$_6$] specimens.

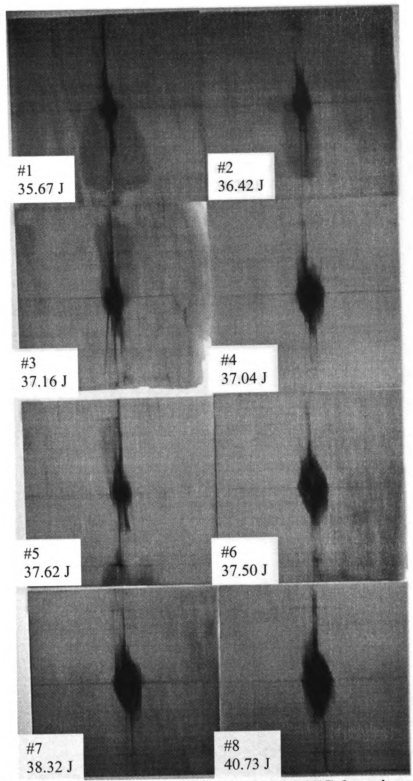

Figure H-4: Bottom view of damage to L[(0/15)$_6$] specimens.

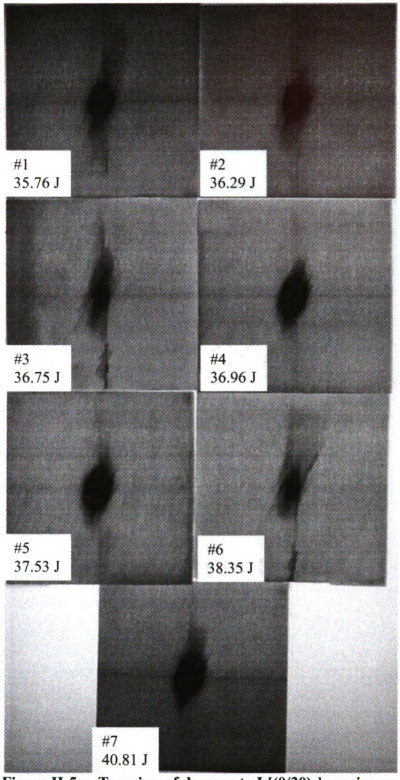

Figure H-5: Top view of damage to L[(0/30)$_6$] specimens.

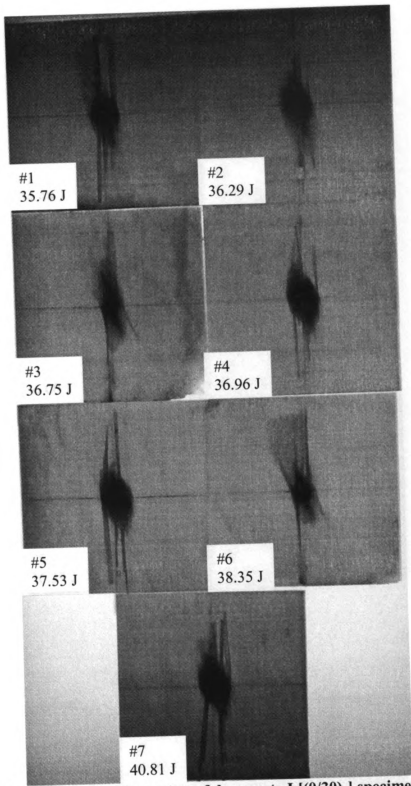

Figure H-6: Bottom view of damage to L[(0/30)$_6$] specimens.

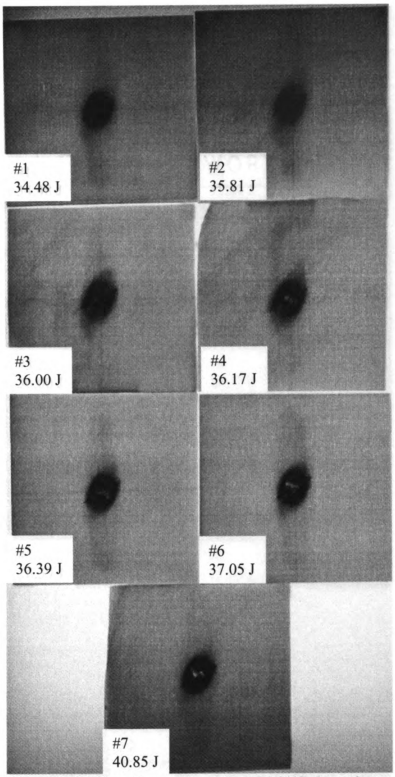

Figure H-7: Top view of damage to L[(0/45)$_6$] specimens.

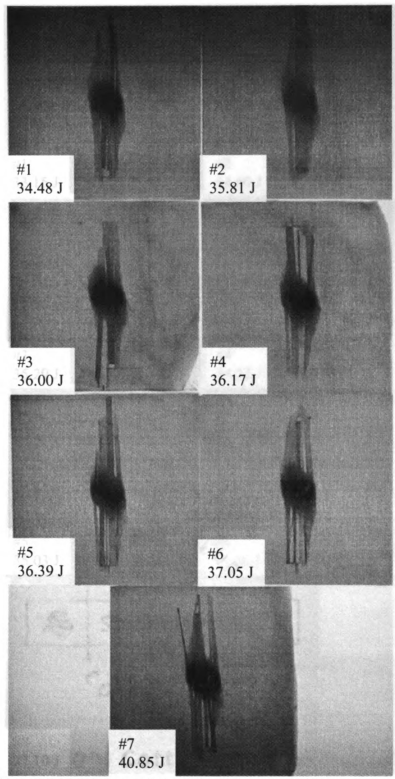

Figure H-8: Bottom view of damage to L[$(0/45)_6$] specimens.

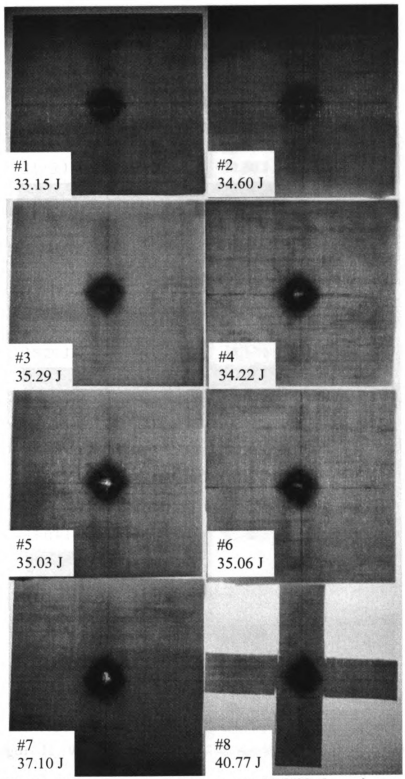

Figure H-9: Top view of damage to L[(0/90)$_6$] specimens.

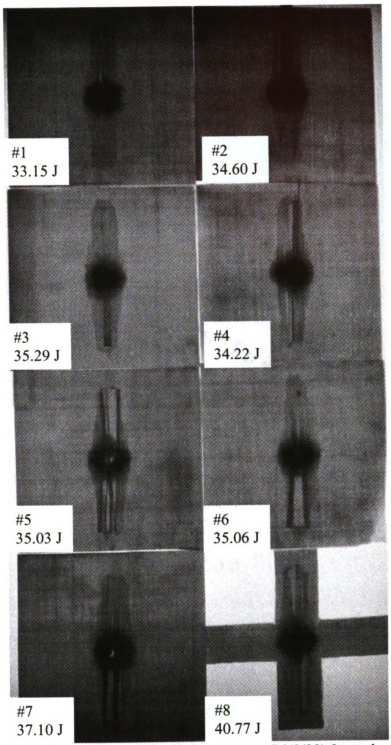

Figure H-10: Bottom view of damage to L[(0/90)$_6$] specimens.

Appendix I

Stitched specimen damage

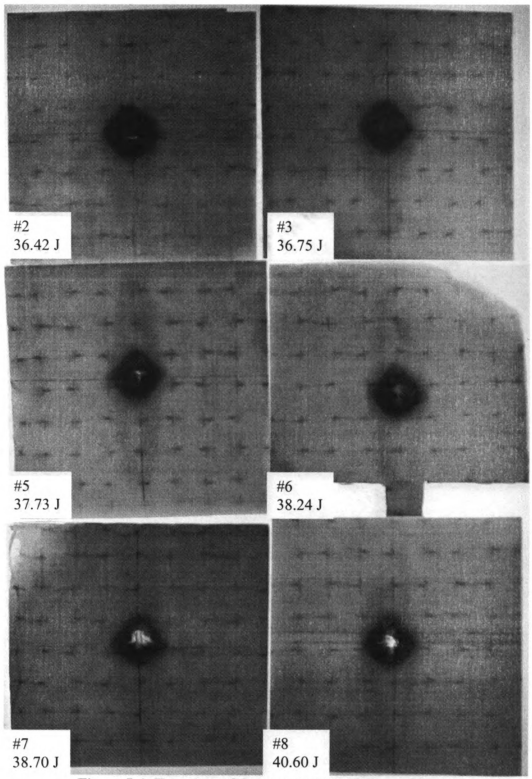

Figure I-1: Top view of damage to S[(0/90)$_6$] specimens.

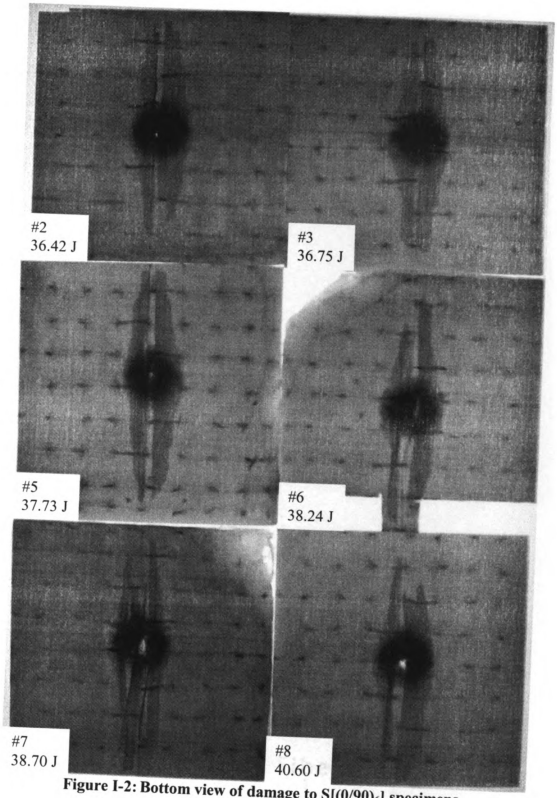

Figure I-2: Bottom view of damage to S[(0/90)$_6$] specimens.

Appendix J

Two-dimensional woven specimen damage

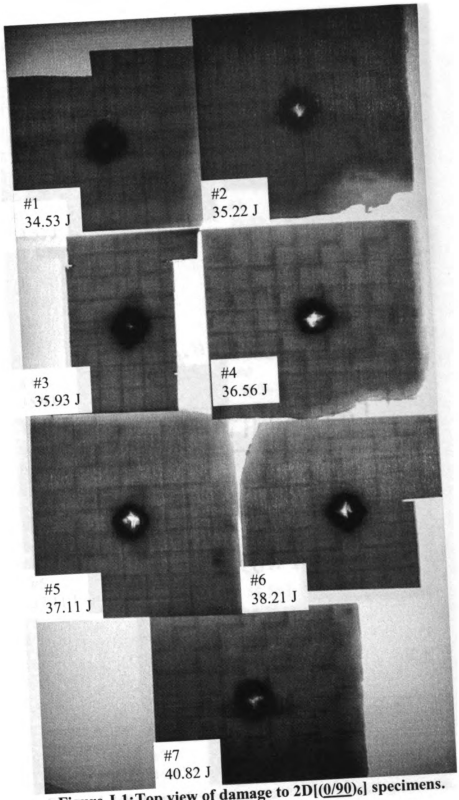

Figure J-1: Top view of damage to 2D[(0/90)$_6$] specimens.

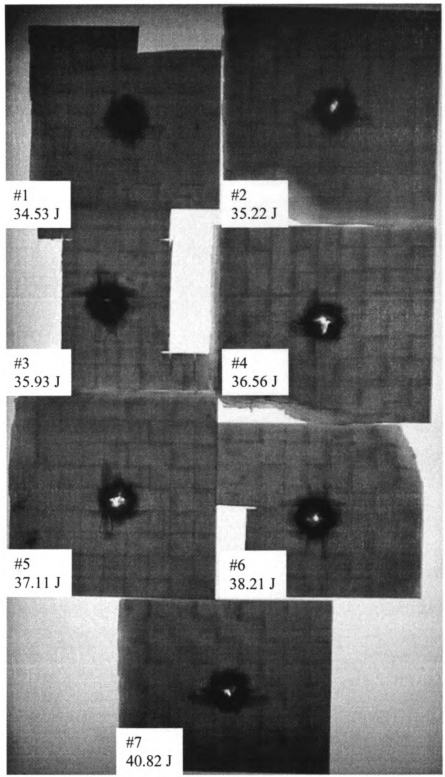

Figure J-2: Bottom view of damage to 2D[$(\underline{0/90})_6$] specimens.

Appendix K

Three-dimensional woven specimen damage

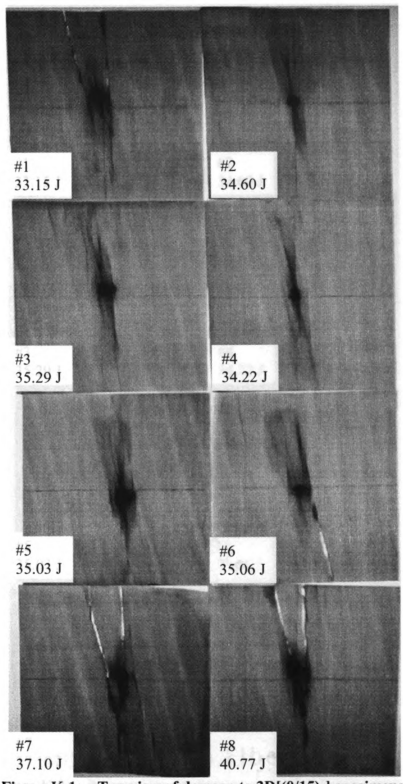

Figure K-1: Top view of damage to 3D[(0/15)$_6$] specimens.

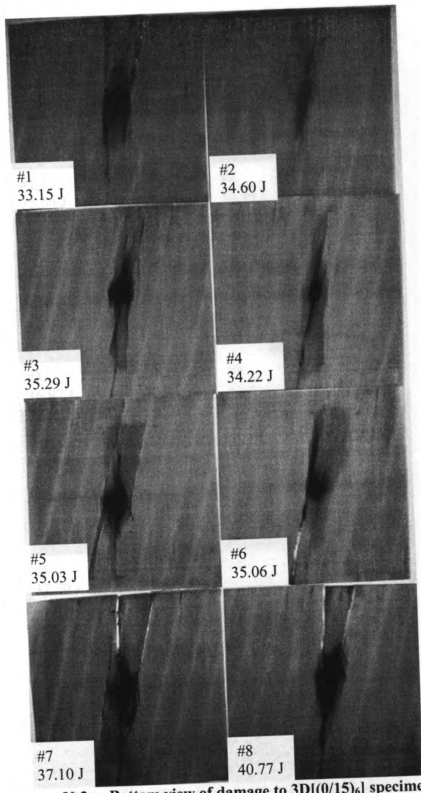

Figure K-2: Bottom view of damage to 3D[(0/15)$_6$] specimens.

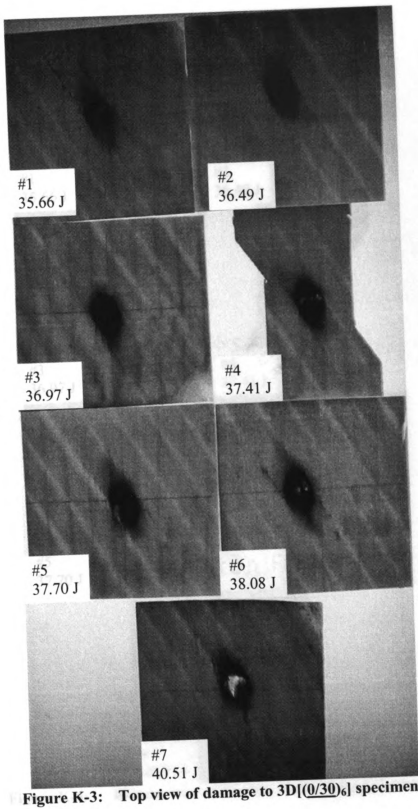

Figure K-3: Top view of damage to 3D[(0/30)$_6$] specimens.

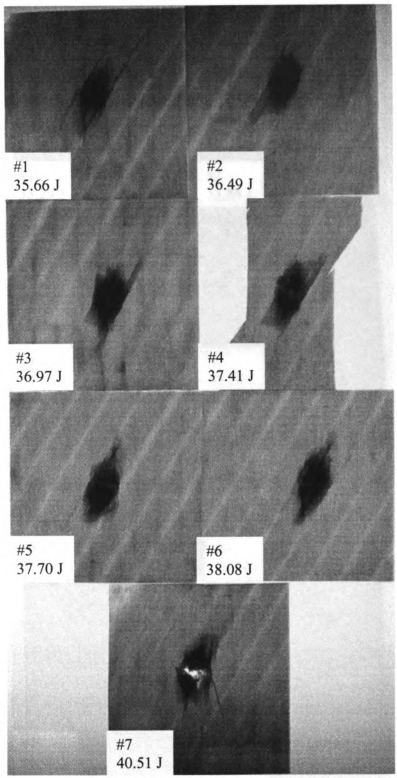

Figure K-4: Bottom view of damage to 3D[(0/30)$_6$] specimens.

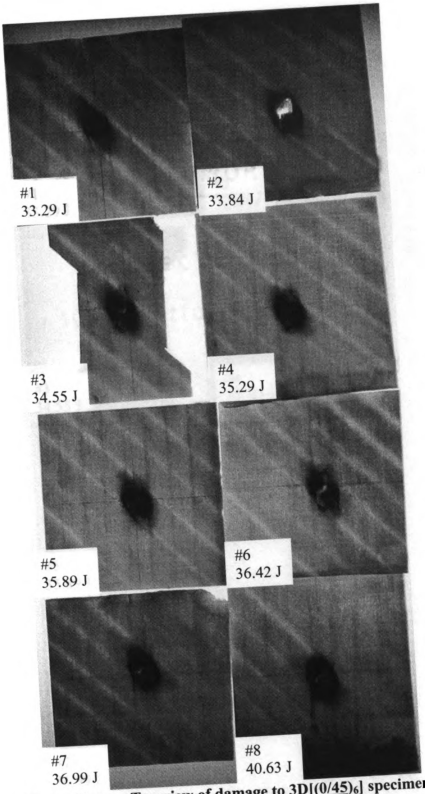

Figure K-5: Top view of damage to 3D[(0/45)$_6$] specimens.

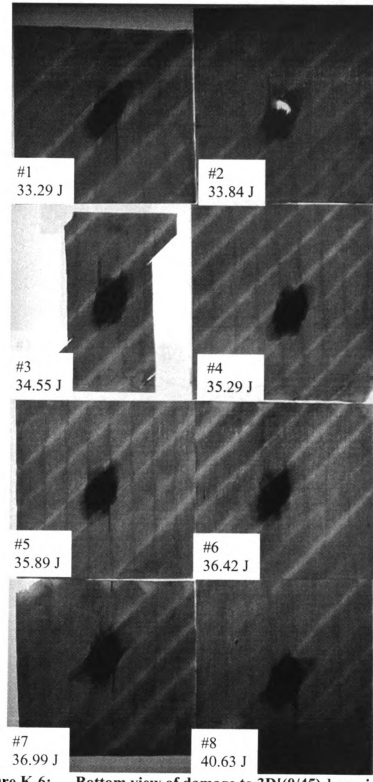

Figure K-6: Bottom view of damage to 3D[(0/45)$_6$] specimens.

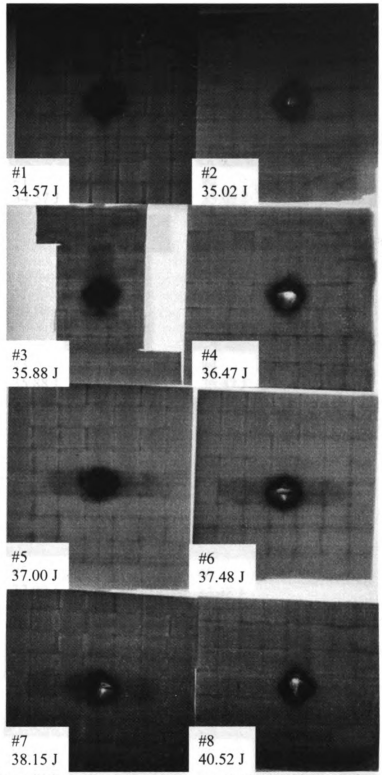

Figure K-7: Top view of damage to 3D[(0/90)$_6$] specimens.

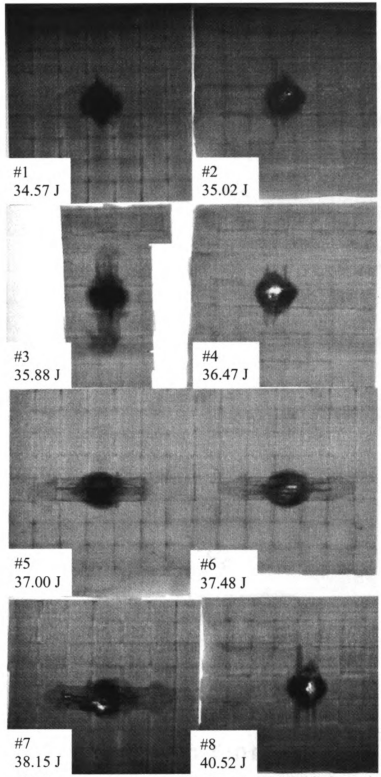

Figure K-8: Bottom view of damage to 3D[(0/90)$_6$] specimens.

References

[1] Jovicic, J., Zavaliangos, A., Ko, F., "Modeling of the Ballistic Behavior of Gradient Design Composite Armors," *Composites Part A*, Vol. 31, 1996, pp. 773-784.

[2] Kim, J.K., Sham, M.L., "Impact and Delamination Failure of Woven-Fabric Composites," *Composites Science and Technology*, Vol. 60, 2000, pp. 745-761.

[3] Davies, G., Hitchings, D., Zhou, G., "Impact Damage and Residual Strengths of Woven Fabric Glass/Polyester Laminates," *Composites Part A*, Vol. 27, 1996, pp. 1147-1156.

[4] Sutherland, L., Soares, C., "Effects of Laminate Thickness and Reinforcement Type on the Impact Behavior of E-Glass/Polyester Laminates," *Composites Science and Technology*, Vol. 59, 1999, pp. 2243-2260.

[5] Liu, D., "Delamination Resistance in Stitched and Unstitched Composite Plates Subjected to Impact Loading," *Journal of Reinforced Plastics and Composites*, Vol. 9, 1990, pp. 59-69.

[6] Richardson, M.O.W., Wisheart, M.J., "Review of Low-Velocity Impact Properties of Composite Materials," *Composites Part A*, Vol. 27A, 1996, pp. 1123-1131.

[7] Davies, G., Hitchings, D., Wang, J., "Prediction of Threshold Impact Energy for Onset of Delamination in Quasi-Isotropic Carbon/Epoxy Composite Laminates Under Low-Velocity Impact," *Composites Science and Technology*, Vol. 60, 2000, pp. 1-7.

[8] Naik, N.K., Meduri, S., "Polymer-Matrix Composites Subjected to Low-Velocity Impact: Effect of Laminate Configuration," *Composites Science and Technology*, Vol. 61, 2001, pp. 1429-1436.

[9] Dickinson, L.C., Farley, G.L., Hinders, M.K., "Translaminar Reinforced Composites: A Review," *Journal of Composites Technology and Research*, Vol. 21, No. 1, 1999, pp. 1178-1202.

[10] Larsson, F., "Damage Tolerance of a Stitched Carbon/Epoxy Laminate," *Composites Part A*, Vol. 28A, 1997, pp. 923-934.

[11] Mouritz, A.P., "Flexural Properties of Stitched GRP Laminates," *Composites Part A*, Vol. 27, 1996, pp. 525-530.

[12] Mouritz, A.P., Bannister, M.K., Falzon, P.J., Leong, K.H., "Review of Applications for Advanced Three-Dimensional Fibre Textile Composites," *Composites Part A*, Vol. 30, 1999, pp. 1445-1461.

[13] Walker, L., Sohn, M.S., Hu, X.Z., "Improving Impact Resistance of Carbon-Fibre Composites Through Interlaminar Reinforcement," *Composites Part A*, Vol. 33, 2002, pp. 893-902.

[14] Naik, N.K., Borade, S.V., Arya, H., Sailendra, M., Prabhu, S.V., "Experimental Studies on Impact Behavior of Woven Fabric Composites: Effect of Impact Parameters," *Journal of Reinforced Plastics and Composites*, Vol. 21, No. 15, 2002, pp. 1362.

[15] Ebeling, T., Hiltner, A., Baer, E., Fraser, I.M., Orton, M.L., "Delamination Failure of a Woven Glass Fiber Composite," *Journal of Composite Materials*, Vol. 31, No. 13, 1997, pp. 1318-1333.

[16] Siow, Y.P., Shim, V.P.W., "An Experimental Study of Low Velocity Impact Damage in Woven Fiber Composites," *Journal of Composite Materials*, Vol. 32, No. 12, 1998, pp. 1178-1202.

[17] Liu, D., Raju, B.B., Dang, X., "Impact Perforation Resistance of Laminated and Assembled Composite Plates," *International Journal of Impact Engineering*, Vol. 24, 2000, pp. 733-746.

[18] Baucom, J.N, Zikry, M.A., "Evolution of Failure Mechanisms in 2D and 3D Woven Composite Systems Under Quasi-Static Perforation," *Journal of Composite Materials*, Vol. 37, No. 18, 2003, pp. 1651-1674.

[19] Liu, D., "Impact Induced Delamination – A View of Bending Stiffness Mismatching," *Journal of Composite Materials*, Vol. 22, 1988, pp. 674-692.